ENERGETIC PARTICLE EVENTS: EFFICIENCY OF INTERPLANETARY SHOCKS AS 50 keV < E < 100 MeV PROTON ACCELERATORS

D. LARIO[1] AND B. SANAHUJA[2]

Departament d'Astronomia i Meteorologia, Universitat de Barcelona, Avinguda Diagonal 647, 08028 Barcelona, Spain

AND

A. M. HERAS

ESA Space Science Department, VILSPA, ESA Satellite Tracking Station, P.O. Box 50727, Villafranca del Castillo, E-28080 Madrid, Spain

ABSTRACT

We have studied the injection rate of shock-accelerated protons in long-lasting particle events by tracing back the magnetohydrodynamic conditions at the shock under which protons are accelerated. This tracing back is carried out by fitting the observed flux and anisotropy profiles at different energies, considering the magnetic connection between the shock and the observer, and modeling the propagation of the shock and of the particles along the interplanetary magnetic field. A focused-diffusion transport equation that includes the effects of adiabatic deceleration and solar wind convection has been used to model the evolution of the particle population. The mean free path and the injection rate have been derived by requiring consistency with the observed flux and anisotropy profiles for different energies, in the upstream region of the events. We have extended the energy range of previous models down to 50 keV and up to ~ 100 MeV. We have analyzed four proton events, representative of west, central meridian, and east scenarios. The spectra of the injection rate of shock-accelerated protons derived for these events show that for energies higher than 2 MeV the shock becomes a less efficient proton accelerator. We have related the derived injection rates to the evolution of the strength of the shock, particularly to the normalized downstream-upstream velocity ratio (VR), the magnetic field ratio, and the angle θ_{Bn}. As a result, we have derived an empirical relation of the injection rate with respect to the normalized velocity ratio ($\log Q \propto$ VR), but we have not succeeded with the other two parameters. The Q(VR) relation allows us to determine the injection rate of shock-accelerated particles along the shock front and throughout its dynamical expansion, reproducing multispacecraft observations for one of the simulated events. This relation allows us to analyze the influence of the corotation effect on the modeled particle flux and anisotropy profiles.

Subject headings: acceleration of particles — interplanetary medium — MHD — shock waves — Sun: particle emission

1. INTRODUCTION

Modeling energetic proton events associated with interplanetary shocks requires two basic components: a suitable description of the propagation of protons through the interplanetary medium and an adequate simulation of the evolution of the interplanetary shock where protons are accelerated. Heras et al. (1992, 1995; hereafter He92 and He95, respectively) have developed a quantitative model that accounts for the main features of these events in the upstream region of the shock. This model is based on the concept of the "cobpoint" (Connecting with the OBserver point), the point at the front of the shock that connects with the observer through the IMF (interplanetary magnetic field) lines; the model has two basic parameters: the mean free path of the protons, $\lambda_{\parallel}$, and the injection rate of shock-accelerated protons into the interplanetary medium,

$Q(r, t)$. From the fitting of the observed flux and first-order anisotropy profiles, for a fixed energy, it is possible to determine Q and $\lambda_{\parallel}$, as well as their evolution until the shock passes the spacecraft. Specifically, it allows us to relate the evolution of Q, for energies between ~ 200 keV and 1.5 MeV, to the evolution of various physical parameters at the shock front. Hereafter, we will use the terms "proton" or "particle" indistinctly, and unless otherwise indicated, "high-energy" will mean $E \gtrsim 2$ MeV.

The transport equation used by He92 and He95 to describe the propagation of energetic protons along the IMF is the focused-diffusion equation derived by Roelof (1969). The diffusion-convection approximation (Parker 1965) is not applicable to the description of large particle events associated with strong interplanetary shocks, because these often show high anisotropies in the upstream region, not only at the onset but also for many hours before the shock passage. These high anisotropies imply that protons are injected continuously into the interplanetary medium after being accelerated at the shock (Heras et al. 1994 and references therein). The injection rate is described

[1] Now at the Space Science Department of ESA, ESTEC, P.O. Box 299, 2200 AG Noordwijk, The Netherlands.

[2] Also at the Institut d'Estudis Espacials de Catalunya. Gran Capità 2, Nexus-201, 08034-Barcelona, Spain.

415

in the model by adding a source term to the transport equation, the function Q mentioned above. Q is identified with the "efficiency" of the shock as a particle accelerator, which comprises the effectiveness of the shock in accelerating protons plus the efficiency of injecting these protons into the interplanetary medium. The injection factor depends on the conditions around the shock; for example, the presence of a turbulent wavy region upstream of the shock or a large background of protons acting as a seed population. The model uses a magnetohydrodynamic (MHD) code to simulate the expansion and propagation of interplanetary shocks, up to 1.1 AU, triggered by solar activity (i.e., Dryer 1994). The evolution of the injection rate Q can be analyzed as a function of the MHD conditions at the shock front and as a function of the assumptions considered by the MHD code to describe the interplanetary shock.

It is generally accepted that interplanetary shocks accelerate particles more efficiently at low than at high energies (Forman & Webb 1985 give a comprehensive review of the acceleration of energetic particles). It is quite usual to see a small peak, if any, on the 1 MeV proton flux at the shock passage, while a jump from 1 to 3 orders of magnitude is observed in the flux at 50 keV. One basic limitation of the focused-diffusion equation used in He92 and He95 is that it does not take into account the effects of adiabatic deceleration or convection by the solar wind; these effects may be important below 800 keV. If, for example, the injection rate at 100 keV is derived by means of this equation, substantial uncertainty is introduced in the values of Q found, because it might include arbitrarily positive (high-energy) or negative (low-energy) contributions due to adiabatic deceleration. A similar discussion involving $\lambda_\parallel$ is given by Ruffolo (1995, hereafter Ru95). Solar wind convection may also have an important influence in determining the onset of an event and the occurrence of the maximum of flux, especially at low energies. For that reason, the focused-diffusion equation should be used judiciously below 500 keV. Ru95 has developed an explicit formula for the focused-diffusion transport of solar cosmic rays, including adiabatic deceleration and solar wind convection effects (a first-order approximation). This equation is more appropriate for describing the transport of low-energy particles than the Roelof (1969) approximation; with it, Ru95 models the transport of solar flare protons (from a fixed source, the Sun). For particle events associated with interplanetary shocks, however, it is necessary to assume that the source of accelerated particles is moving jointly with the shock, which demands a different approach for the numerical resolution of the transport equation.

The acceleration of low-energy protons is reasonably well understood in terms of either shock drift acceleration or diffusive shock acceleration (with MHD turbulence). Nevertheless, how these processes work above a few MeV is not clear, since it is expected that the efficiency of the shock decreases rapidly with the energy (e.g., Kallenrode 1996 and references therein). Since the He92 model can evaluate this efficiency, it is worth extending the range of applicability of the model in order to analyze what happens at such high energies. Furthermore, based on these results, Lario et al. (1995b) suggest that the large-scale features of the flux and anisotropy profiles for different events can be easily adjusted, assuming a reasonable functional dependence of the injection rate at the cobpoint. Consequently, we have developed a model that allows us to extend the range of applica-

bility to energies between 50 keV and 100 MeV, with a more reduced set of parameters.

The observed flux and anisotropy profiles of energetic particle events depend on both how efficiently protons are accelerated, and how the IMF irregularities modulate this population during its journey. Lario, Sanahuja, & Heras (1995a) show examples of particle flux profiles that can be adjusted in different ways if only one of those aspects is considered. Moreover, the efficiency of the acceleration depends on the MHD strength of the shock at the cobpoint. This strength could either diminish, because of the shock expansion in the interplanetary medium (or because the cobpoint slides clockwise to the right wing of the shock), or increase, when the cobpoint moves from the left wing to the central region of the shock. It is then possible that a region of the shock could accelerate protons up to 20 MeV at 0.1 AU, but only to 500 keV when it reaches 1 AU. This scenario for particle acceleration at the shock and their further propagation upstream has already been qualitatively depicted using statistical studies and multispacecraft analysis of specific events (e.g., Cane, Reames, & von Rosenvinge 1988; Domingo, Sanahuja, & Heras 1989; Reames, Barbier, & Ng 1996). Although there is an extended consensus about it, the details of how the MHD conditions at the front of the shock translate into an "efficiency" in particle acceleration, and of how it evolves as the shock expands, are neither completely clear nor quantified as yet. Therefore, we would like to focus on an analysis of the efficiency of the shock as an accelerator of protons, $Q(r, t)$. The other main parameter of the model, the mean free path, is tuned to fit the observations and theoretical predictions, but the values obtained will not be discussed in detail. We refer to other studies on the influence of $\lambda_\parallel$ on the interplanetary transport of protons (e.g., Beeck et al. 1990). Our aim is to deconvolve the effects of particle transport on the flux, in order to derive the efficiency of the shock as an injector of protons into the interplanetary medium.

Kallenrode & Wibberenz (1997) have extended a model formerly used to analyze solar particle events (see, for example, Beeck & Wibberenz 1986 and references therein) to describe the influence of the shock as a moving accelerator of particles. The physical basis of this model is the same as in He92 and He95, since they use Roelof's transport equation to describe particle propagation, and include a source term for particles moving along the IMF line; furthermore, this source term is derived by fitting the flux profile independently at each energy. The main differences are the handy separation of the source term in two contributions, radial and azimuthal along the shock front, the assumption that particles propagate downstream spiraling in an Archimedian IMF, and the assumption that the shock can be represented by a segment of a circle propagating at a constant speed, which allows the unhindered motion of the particles across it. There is also an arbitrary parameter (r_{start}) used to fix the connecting time of the observer with the shock front when high-energy particles arrive with too much delay. Nevertheless, the shock does not evolve at constant velocity, and its central part does not propagate at the same speed as the wings; the IMF downstream of the shock cannot be represented by an Archimedian spiral, and particles cannot propagate freely across the shock, especially at low energy. This model cannot be adequately applied to low energies, since the particle transport equa-

tion does not take into account adiabatic deceleration and solar wind convection.

The main justification for the set of assumptions made by Kallenrode & Wibberenz (1997) is the result of the statistical study of 44 particle events (Kallenrode 1997a), and individual analysis of several of these events (Kallenrode 1997b). This statistical study cannot yield clear quantitative conclusions about the injection rate, its energy spectrum, or its evolution. The most probable reasons for this are that (1) shock-accelerated particles come from different regions along the front of the shock, showing different MHD conditions due to shock expansion that this model ignores; (2) statistical analysis is not able to cancel out the specificity of each event; and (3) the source term cannot always be unequivocally described by a combination of radial and azimuthal dependence, as stated by Kallenrode (1997b). On the other hand, the evolution of the injection rate derived for a large portion of the events presented by Kallenrode (1997b) should be taken with caution, because many of the fits performed for the flux and anisotropy profiles display large discrepancies (more than 1 order of magnitude) with observations, for long periods (i.e., Figs. 1, 5, or 8 of that paper). There is also no discussion or justification of how these discrepancies affect the injection rate derived and its evolution.

The improvements now included in the transport equation over that of He95 allow us to reduce the parameters of the model and to improve the description of particle propagation. We also propose a different way to relate the evolution of the injection rate of shock-accelerated particles to the dynamic properties of the shock. The new model yields a quantification of the injection rate, its energy spectrum, and its evolution. We will discuss the assumptions of the model and the influence of the shock modeling on the results. We will proceed as follows: in § 2 we briefly describe the new numerical procedure for solving the transport equation, how we proceed to derive the injection rate of shock-accelerated particles from the fitting of flux and anisotropy profiles, and the role of the shock front as a source of particles. In § 3 we briefly review the observational features of the four particle events to be modeled. In § 4 we present the fits performed for these events and discuss the mean features of the injection rate and of its energy spectrum derived from those fittings. In § 5 we relate the evolution of the injection rate to the strength of the shock. We discuss this dependence and other aspects of the depicted scenario that could make the interpretation of these results or their comparison with the observations difficult. We also discuss the influence of corotation. Finally, in § 6 we present the conclusions of the paper.

2. THE NUMERICAL MODEL

2.1. *Propagation of Particles*

Our goal is to study the evolution of the injection rate of protons accelerated at the front of interplanetary shocks, for a wide range of energies from 50 keV to 100 MeV. Shock-accelerated particles are considered to propagate in a magnetic flux tube from the shock front up to the observer. Their transport is modulated by the characteristics of the IMF and of the solar wind, which have different effects depending on the energy of the particles. We describe particle propagation by means of the following transport equation (Ru95), written in mixed coordinates:

$$\frac{\partial F(t, \mu, r, p)}{\partial t} = -\cos \psi \frac{\partial}{\partial r}$$

$$\times \left\{ \left[v\mu + \left(1 - \mu^2 \frac{v^2}{c^2} \right) v_{sw} \sec \psi \right] F(t, \mu, r, p) \right\}$$

$$- \frac{\partial}{\partial \mu} \left\{ \left[\frac{v}{2L(r)} \left(1 + \mu \frac{v_{sw}}{v} \sec \psi - \mu \frac{v_{sw} v}{c^2} \sec \psi \right) \right. \right.$$

$$\left. + v_{sw} \left(\cos \psi \frac{d}{dr} \sec \psi \right) \mu \right] (1 - \mu^2) F(t, \mu, r, p) \right\}$$

$$+ \frac{\partial}{\partial \mu} \left\{ D_{\mu\mu} \frac{\partial}{\partial \mu} \left[\left(1 - \mu \frac{v_{sw} v}{c^2} \sec \psi \right) F(t, \mu, r, p) \right] \right\}$$

$$+ \frac{\partial}{\partial p} \left\{ p v_{sw} \left[\frac{\sec \psi}{2L(r)} (1 - \mu^2) + \cos \psi \frac{d}{dr} (\sec \psi) \mu^2 \right] \right.$$

$$\left. \times F(t, \mu, r, p) \right\} + G(t, \mu, r, p) , \qquad (1)$$

where p denotes the particle momentum, μ is the cosine of the pitch angle, v is the velocity of the particles, r is the heliocentric distance, t the time, ψ is the angle between the radial direction and the magnetic field B, L is the focusing length, $D_{\mu\mu}$ is the diffusion coefficient in μ-space, and v_{sw} is the radial solar wind velocity relative to a fixed frame. The particle phase-space distribution function, f, is related to the distribution function of protons inside the flux tube, F, by $F(t, \mu, r, p) = A(r)f(t, \mu, r, p)$ (Ng & Wong 1979), where $A(r)$ is the cross-sectional area of the magnetic flux tube. G represents a local source of protons, directly related to the injection rate of protons in the phase-space, Q, by $G(r, t) = A(r)Q(r, t)$, with $A(r)$ estimated at the point where the injection of protons is occurring.

The coordinates p, v, and μ refer to the local solar wind frame comoving with the inhomogeneities of the IMF, while z, r, and t refer to a frame fixed at the Sun. The first term on the right-hand side of equation (1) represents the streaming and convection, and the second term is the usual expression for adiabatic focusing. The third term represents the pitch-angle scattering, and the fourth term represents the adiabatic deceleration. The two main differences between equation (1) and equation (11) of Ru95 are the inclusion of the source term $G(t, \mu, r, p)$, which gives the injection of protons at the cobpoint, and the use of the r coordinate instead of the distance z along the magnetic field line ($dr = dz \cos \psi$). The use of the radial coordinate is forced because the MHD simulation provides the radial position of the shock and the structure of the IMF lines with its own r-grid. Using r instead of z allows us to couple the grid of the MHD simulation for the shock propagation and the grid used to solve equation (1).

Assuming a Parker field, we have $L = r/\cos \psi(1 + \cos^2 \psi)$, $\tan \psi = \Omega r/v_{sw}$, and $A = A(r_0)r^2/(1 + \tan^2 \psi)^{1/2}$, where Ω is the angular velocity of the solar rotation and r_0 is a given radial distance. For other magnetic field configurations, these equations would require more complicated expressions; in fact, they would require a complex numerical description. Therefore, this approximation can only be applied when the upstream solar wind is not highly perturbed.

To describe the interaction between energetic particles and IMF irregularities, we adopt the approximation of

pitch-angle scattering. For the pitch-angle diffusion coefficient we use the standard model (Jokipii 1971), $D_{\mu\mu} = \mathscr{A} \, |\mu|^{q-1}(1 - \mu^2)$. $\mathscr{A}$ is a constant that depends on the particle charge, mass, and velocity, and on the level of the IMF fluctuations, and q is the spectral index of the field power spectrum. Following the quasi-linear theory (QLT) approximation (Jokipii 1966), we take $\mathscr{A} = 3v/2\lambda_{\parallel}(4 - q)(2 - q)$, and for consistency we assume for $\lambda_{\parallel}$ a dependence on the rigidity, $\lambda_{\parallel} \propto R^{2-q}$ (Hasselmann & Wibberenz 1970). For each event, the value of q is derived from *ISEE 3* IMF data; a frequently quoted value is $q = 1.6$ (Kunow et al. 1991). This approximation might be subject to correction or improvement, but this would have little influence on the fit performed to the particle flux and anisotropy profiles. Several corrections have recently been suggested. For example, Ng & Reames (1995) suggest an extended QLT that takes into account the distribution of the medium-scale background magnetic field, eliminating the resonance gap for very low energy protons (<25 keV) at pitch angles around $90°$. Since our lowest energy channel considered is above 25 keV and our numerical scheme does not evaluate the coefficient $D_{\mu\mu}$ at $\mu = 0$, we do not consider this extension. Bieber, Wanner, & Matthaeus (1996) show that the turbulence regime observed in the IMF is a composite of the slab turbulence and the two-dimensional turbulence; this second component contributes to the level of turbulence measured, but it does not contribute to resonant scattering of the particles. This is an important result, but we have not included this variable in our modeling because possible changes in q have small influence on the anisotropy derived, and thus on the mean free path (see, e.g., Fig. 5 of He92). Furthermore, the ratio between those components of the turbulence can largely change between different events (Bieber et al. 1996). In our model, this variable would simply be an extra parameter, without leading to any significant real improvement in the results.

The transport equation (1) is solved by applying a time-splitting method that separates this equation into four one-dimensional equations (Lario 1997 describes the numerical procedure in detail). The grid of integration extends in time, space, pitch angle, and momentum, $(t, \mu, r, \log p)$. This grid has absorbing outer and inner boundaries in radial distance (RE and RI, respectively); therefore, particles are allowed to flow out, but the influx is set to zero; that is, $F(t, \mu, r, p) = 0$ when $\mu \leq 0$ (at RI) and when $\mu \geq 0$ (at RE). The outer boundary is set $\gtrsim 3$ AU from the inner boundary, sufficiently far from the Sun and from the observer's position so that it has no effect on the distribution of particles. The four one-dimensional equations are solved using a number of finite-difference methods (first- and second-order, centered/not centered, and upwind/downwind schemes), depending on the characteristics of each equation at each time step. The procedure has been corrected for numerical diffusion by means of a weighted average of the flux computed by a lower order scheme and a higher order scheme (Zalesak 1979). Zalesak's technique of antidiffusion flux correction largely reduces the effects of numerical diffusion.

To compute the effect of adiabatic deceleration, it is necessary to interpolate the distribution function at two adjacent energies (see details in Ru95). Ru95 discusses two ways to compute this, depending on the physical situation: (1) interpolating at equal distance traveled by the particles, or (2) interpolating at a given time. In our case, the continuous injection of particles from the shock leads to the second possibility, since the distribution functions $F(t, \mu, r, p)$

at two different energies are more similar at a given time than at equal distance traveled. For the simulations shown in § 4, we have adopted a time step of 0.01 hr, an r-grid spacing of 0.01 AU, a μ-grid spacing equal to $\frac{1}{8}$, and a momentum step of 0.104 (p in MeV/c). To assess the method, we have tested the code under different conditions and in the diffusion limit. Lario, Sanahuja, & Heras (1997) give a brief description of the performed tests; a full explanation of them can be found in Lario (1997).

To fit the particle flux and anisotropy profiles observed by the spacecraft, it is assumed that the protons are injected from the cobpoint and propagate along the magnetic flux tube connecting the observer to the cobpoint. As the shock expands, the observer establishes magnetic connection to different regions of the shock front; therefore, the cobpoint slides along the shock front. The successive injections of particles from the cobpoint fill the magnetic flux tube where the observer is located. We consider that this flux tube is unique throughout the event; that is, the particles injected from the cobpoint as it moves along the shock front become part of the particle population within the same magnetic flux tube. The inclusion of different flux tubes filled with particles coming from different parts of the shock front and crossing the observer position will be considered in § 5.3.

The procedure for fitting the particle and anisotropy profiles is as follows. We fit particle flux and anisotropy profiles in the upstream region for one energy channel, usually at ~ 1 MeV. This yields the $\lambda_{\parallel}$ and G values for this energy, as well as their evolution. Then, assuming that the functional dependence of G on the energy is a power law ($G \propto E^{-\gamma}$), we use the spectral index γ to obtain the best fit for fluxes and anisotropies at lower energies. The injection rate Q is calculated through the dependence on $A(r)$ and the change to differential flux units. In all cases, the mean free path at different energies is directly given by the QLT dependence of $\lambda_{\parallel}$, provided that the value of q is known from the magnetic field observations. At high energy, each channel has been fitted independently, without assuming any energy dependence for G. In § 4 we will see that the spectral index at high energy must be greater than at low energy. Therefore, this model requires only four basic parameters to fit nine or ten energy channels between 100 keV and 100 MeV, while the number of free parameters is much higher when the profiles are adjusted independently for each energy channel modeled (as is usually done). It is worth pointing out that for some events (see discussion in § 4.2), a turbulent foreshock region is required in order to simultaneously fit particle flux and anisotropy profiles. This is represented by a region of a certain width in front of the shock, characterized by a mean free path ($\lambda_{\parallel c}$) smaller than the mean free path in the rest of the upstream medium. The significance of $\lambda_{\parallel c}$ is discussed in He92 and in Beeck & Sanderson (1989). This represents an additional parameter of the model necessary to simulate simultaneously particle and anisotropy profiles in some particle events.

The low-energy profiles ($\lesssim 1.5$ MeV) have been calculated using a momentum grid that corresponds to the geometric mean energy of each channel. At these energies, the channels are narrow enough that the geometric mean of the window gives a good description of the whole channel. Since the energy windows at high energy are considerably wider than at low energy, we have adopted a wider momentum spacing, also taking into consideration the geometric mean energy of each channel. This implies that the fit at high energy is less accurate than at low energy. This is a

source of uncertainty, because in a west event, for example, the fit to the flux for an energy channel extending from 4 to 57 MeV corresponds to a 15 MeV proton flux. Nevertheless, at the onset of the event, the profile is dominated by the faster 57 MeV protons, while later the 4 MeV protons shape the profile because they are more abundant. It is possible to use a finer grid of momenta, but this would require knowing, a priori, the energy spectrum of Q. An alternative is to postulate in advance an energy spectrum for this energy window, but the injection rate is very sensitive to such an assumption, and there is no way to determine how much more abundant the 4 MeV protons are with respect to the 57 MeV protons. We have preferred to fit the profiles at high energy independently, channel by channel; then the derived spectral index results from a simple fit of the points at high energy and at ~ 1 MeV independently.

2.2. Evolution of the Shock

The MHD model used for the shock propagation is the same as in He92. This model reproduces the plasma and magnetic field data supplied by the spacecraft, as well as the arrival time of the shock at different positions. It has been clearly and extensively laid out in the literature, with all its assumptions. We refer the reader to former studies (He92) for details of the procedure (see also Smith & Dryer 1990). Recently, this model has been compared to another numerical code (Vandas et al. 1997) and found to be in good agreement. This code gives a dynamical description of the propagation of an interplanetary shock between 18 $R_\odot$ and 220 $R_\odot$ from the Sun, the main uncertainties coming from the initial conditions taken at the inner boundary. Gopalswamy et al. (1998) suggest that the proxy used to specify the initial conditions of the input pulse (metric type II shock velocity) that drives the shock is not valid. Transient interplanetary shocks are driven by coronal mass ejections (CMEs) (Cane, Sheeley, & Howard 1987); however, the behavior of these shocks in the corona is different (or is thought to be different) from their behavior in the interplanetary medium (Cliver et al. 1995; Cane 1997). Since the transition of these shocks from the corona to the interplanetary medium is not clear, it is difficult to establish the initial conditions of a shock below 18 $R_\odot$. At this distance, we characterize the shock by a pulse of a certain width, velocity, and duration, where the Rankine-Hugoniot conditions are satisfied. What happens below this boundary remains masked to our model. The assumptions considered to initiate the simulation of the shock are the time of the injection (given by the time of the solar activity associated with the event plus the time spent by the shock to travel up to 18 $R_\odot$) and the direction of injection (given by the solar activity site). Plasma and magnetic field observations from the *ISEE 3*, *Helios 1*, or *Helios 2* spacecraft, depending on their location and the availability of the data, are used to secure adequate initial conditions for the shock propagation, reproducing the time of the shock arrival at the spacecraft and the plasma discontinuity values at the shock passage.

From the simulation of the propagation of the shock, we can estimate its MHD strength at each point of the front, and particularly at the cobpoint. We characterize this strength by the downstream/upstream normalized velocity ratio, VR $= [V_r(d) - V_r(u)]/V_r(u)$, and the magnetic field ratio, BR $= |B(d)|/|B(u)|$, where u and d stand for the values upstream and downstream of the front, respectively, measured in a frame fixed at the Sun. Another relevant variable is θ_{Bn}, the angle between the IMF upstream of the shock and the normal to the shock front. The evolution of VR, BR, and θ_{Bn} is followed once the magnetic connection with the observer is established at $t = t_c$ (t_c being the connecting time), up to the passage of the shock by the observer's position. The determination of the shock parameters at the wings or when the shock is weak (i.e., when BR $\simeq 1$ or VR is small) has been improved over former works (He95). In these situations, it is not easy to identify the zones in which the variables should be evaluated, because of the small jump on plasma parameters that the shock represents. The upstream zone has been located at the radial positions where plasma values start to increase from the background, while the downstream region has been located at the point where plasma values stop increasing (see Lario 1997 for details). The identification of the limits of the shock and its effects on particle population are not easy to define. The interaction of a particle with a plasma discontinuity depends on the energy of the particle. As a consequence, it is possible that a shock could efficiently accelerate low-energy particles at its wings while becoming an inefficient accelerator at high energy. Or, a low-energy particle could "see" a discontinuity on the plasma and magnetic field as a shock, while a high-energy particle will "see" just a small irregularity. In these conditions, the evolution of the cobpoint that this dynamical model yields (i.e., where the wings could deform or slow down) has more physical significance than an evolution derived solely by assuming a half-circumferential shock propagating at the mean transit speed, with ad hoc locations for the starting and ending injection of particles, and is, physically, much better than any description based on cartoons.

3. OBSERVATIONAL FEATURES OF THE EVENTS

We have applied the model to four intense particle events detected by *ISEE 3*. Three of them have already been modeled (He95), but now the energy range explored has been extended down to ~ 50 keV and up to ~ 100 MeV (the precise values depending on the observational data available). More important, the fitting will directly yield the energy spectra of the injection rate of shock-accelerated particles. In this way, we can compare the results obtained with those derived for the 0.1–1 MeV range. The fourth particle event is associated with an interplanetary shock observed by the *ISEE 3* spacecraft at 0748 UT on 1981 April 26. We will refer to these particle events as the "WF event" (West Fast event, 1981 April 26), the "WS event" (West Slow event, 1981 December 8), the "E event" (East event, 1979 February 18), and the "CM event" (Central Meridian event, 1979 April 24). Hereafter, we will designate the shocks associated with each of these events as the WF, WS, E, and CM shocks, respectively. Modeling the WF event will permit us to compare the evolution of Q over a long time (1.5–2.5 days), and to analyze the influence on Q of different hypotheses of the model.

Among the large energetic particle west events observed by *ISEE 3* between 1978 September and 1982 February, the WF event is one of the few for which the anisotropy has been computed for a large number (seven) of low-energy channels, that shows a relatively stable IMF in the upstream region, and that shows signatures of both coronal and interplanetary accelerated matter. This event is associated with a 2B flare located 18° north, 50° west, on 1981 April 24, between 1355 UT and 1408 UT (Sanahuja & Domingo 1982), showing a long-duration X-ray event and

type II radio emission (Cane 1985). No CME has been reported around that time, although Solwind observed a CME 2 hr earlier, located at 10° south (R. Howard 1996, private communication). The interplanetary shock is associated with an interplanetary type II event (Pinter et al. 1982; Cane 1985). This hectometric radio emission seems to originate at about 10 $R_\odot$ (Cane 1997 and references therein); particularly for this event, Pinter et al. (1982) found an average velocity of propagation of 2030 km s^{-1} at 0.05 AU, and of 1480 km s^{-1} at 0.1 AU. These values should be taken as approximate, because of the simplifications assumed when derived (see Pinter's comments). The average velocity of propagation of the shock, between the Sun and *ISEE 3*, is 970 km s^{-1}; consequently, the shock undergoes significant deceleration during its journey to 1 AU.

The WF event is a well-connected event, showing an enrichment of the Fe/O ratio (2–12 MeV amu^{-1}; Reames, Cane, & von Rosenvinge 1990) in the early phase of the event. This ratio stays high until the high-energy (4–6 MeV) proton flux reached its maximum, ~ 5 hr after the onset of the event (a signature of impulsive events; Reames 1990); later, it decreases to the value found in gradual events. Klecker (1983) and Cane, Reames, & von Rosenvinge (1991) interpret this evolution as a composite of flare-associated ion populations at the onset phase, followed by an interplanetary shock-accelerated population (see also Miller & Viñas 1993). This event is one of the few cases identified (Reames et al. 1990) that has impulsive and gradual components; following Cliver's (1996) terminology, it is a mixed-impulsive event. Finally, a particular characteristic of this event is that between 50 and 500 keV, it shows magnetic flux tubes with a background proton population of magnetospheric origin (highly anisotropic flux spikes), and also from a former event (quasi-isotropic).

While the WF event was developing, *Helios 1* (located at ~ 0.8 AU, $\sim 105°$ east) observed two proton (5–10 MeV) flux enhancements at the beginning of April 26. In principle, one of them might be related to the shock observed by *ISEE 3*, because *Helios 1* should be magnetically connected to the Sun at $\sim 60°$ east. This is highly improbable, except if the shock was really huge ($\gtrsim 220°$, twice from 50° west to 60° east), and strong enough to maintain active shock-particle acceleration at its right wing for an extended period of time. It is more reasonable to assume that the particle events observed by *Helios 1* were associated with one of the several solar active phenomena developing between 10° and 90° east at that time (Woo & Schwenn 1991); in particular, there were two intense flares erupting at 0633 UT (54° east) and at 0718 UT (58° east) on April 26. Otherwise, such a wide shock ought to be related to a large CME, for which there is no observational evidence (i.e., Sheeley et al. 1985). Furthermore, Woo & Schwenn (1991) report Doppler scintillation observations by *Pioneer Venus* for this period, and relate them to the interplanetary disturbances detected by *Helios 1*. Looking at these observations, it is clear that the scintillation transient observed in early April 25 has no relation to the shock observed by *Helios 1* (except if it propagates very fast at ~ 0.7 AU), and it is even more improbable that this could be the same shock as observed by *ISEE 3* on April 26.

Low-energy data come from the DFH instrument on board the *ISEE 3* spacecraft (Balogh et al. 1978; Sanderson, Reinhard, & Wenzel 1981). High-energy data have been extracted from the *ISEE 3* data pool, except for the flux in the 26.5–147 MeV channel, for which the raw *ISEE 3* data

were kindly provided by D. Ruffolo (1994, private communication). The anisotropy of low-energy fluxes is derived as described in Sanderson et al. (1985), while at high energy it is calculated from the sector count rates, taking into account the characteristics of the detector. It has not been possible to compute all the anisotropies at high energy, because either the fluxes were too low, the integration time was too long (from which unreasonable values result), or the counts per sector were not available. For the E event, anisotropy profiles have been calculated using the count rates in a very wide energy range (26.5–147 MeV) and an integration time of 10 minutes. The method used is an application of Sanderson et al. (1985) for one detector with eight sectors on a plane, and correcting for the Compton-Getting effect (Lario 1997).

4. DERIVING THE INJECTION RATE AND ITS SPECTRUM

4.1. *Evolution of the Shocks*

The shocks associated with the CM, E, and WS events have been modeled as in He92 and He95. The propagation of the WF shock from the Sun to 1.1 AU has been simulated assuming initial conditions for the MHD pulse that reproduce the plasma velocity and magnetic field values observed by *ISEE 3*. Unfortunately, at this time *Helios 1* was not adequately located to be able to further constrain these conditions; *Prognoz 8* also detected this shock, but it was orbiting the Earth and thus was too close to *ISEE 3* to provide supplementary useful information. The hectometric type II radio emission observed in association with this event gives clues as to how the shock propagates, but it does not help us to decide how wide (ω) the initial pulse should be. We have assumed two different initial conditions for the initial shock: WF1 ($V_s = 1775$ km s^{-1}, $\omega = 60°$), and WF2 ($V_s = 1350$ km s^{-1}, $\omega = 168°$), with the time duration of the shock pulse $\tau = 2$ hr in both cases. The WF1 shock better reproduces the values of the velocity associated with the type II emission, while the WF2 shock more accurately fits the magnetic jump ratio observed at *ISEE 3*; at 1 AU, WF2 produces a shock front wider than the shock for the WF1 case. It would be possible to merge both conditions into one case, but as the shock data cannot be checked by another spacecraft in this event, we have considered both cases for the evolution of this shock. This will also allow us to study how the topology of the shock front influences the evolution of Q, and its dependence on the input shock conditions.

Figure 1 shows one snapshot of the simulation of the propagation for the WF1 and WF2 shocks, 25 hr after the maximum of the solar activity ($t = 0$) that originated the event. The shock front is located within the steep density gradient of the isocontours [$\log_{10}$ (density) cm^{-3}]. The inner boundary only permits us to establish an upper limit for the moment at which the magnetic connection between *ISEE 3* and the shock front was established, t_c, although the expected value should be zero, or very close. We have considered $t_c = 5$ hr; in this way, we make sure that the shock has enough time to reach the inner boundary of the MHD simulation, and a stable magnetic connection perfectly delineated by the MHD model is established. The transit time from the Sun to *ISEE 3* given by the model is 42.00 hr for the WF1 shock, and 41.43 hr for the WF2 shock. The evolution of VR and BR at the cobpoint for these two cases is shown in the two upper panels of Figure 2. The lower panels give the position of the cobpoint at the shock front, identified by its distance to the Sun and the angle with
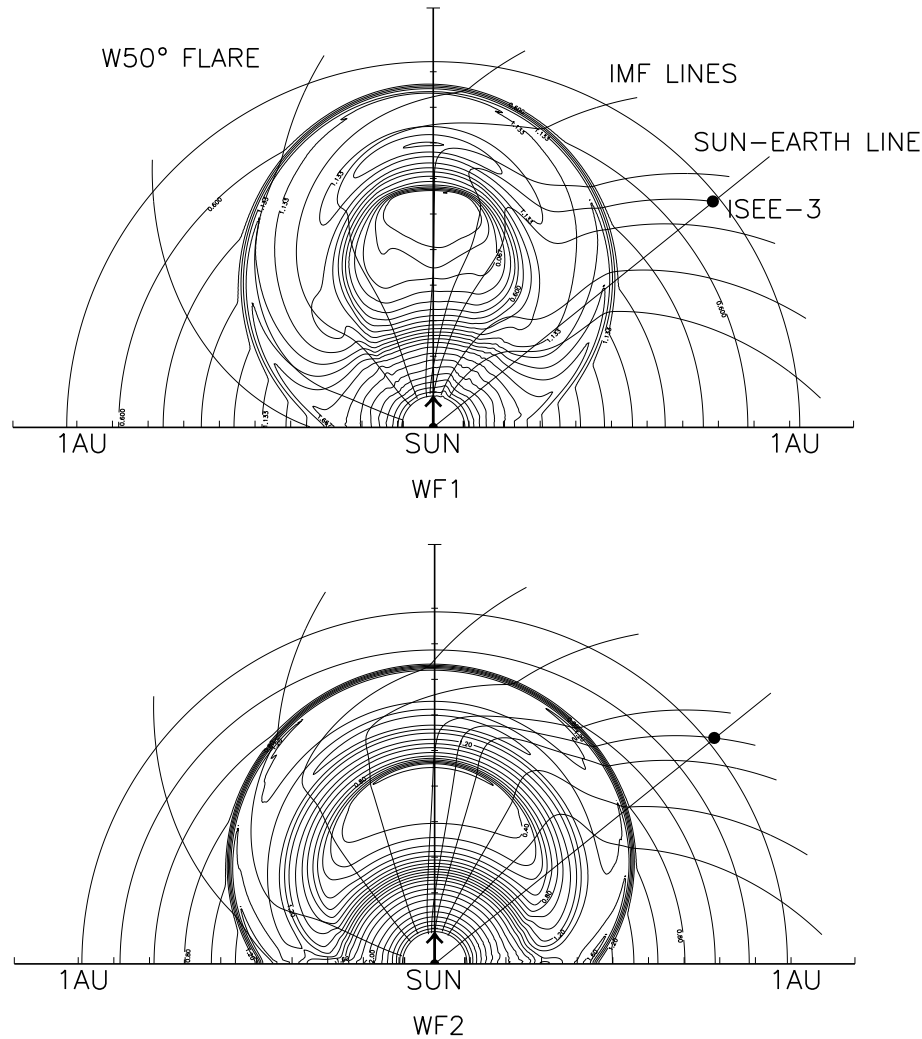
Fig. 1.—Snapshots of the simulation of the propagation of the WF1 (*upper panel*) and WF2 (*lower panel*) cases for the WF event. The log (density) contours (particles cm^{-3}) and some IMF lines are represented. The shock is located within the steep gradients. The arrow indicates the position of the solar source.
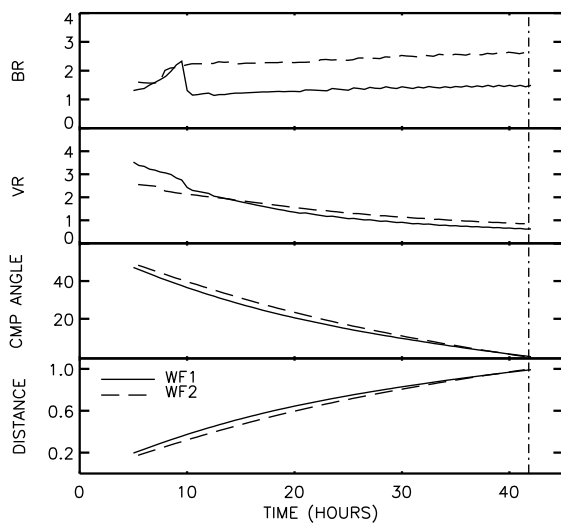

Fig. 2.—WF event. Evolution of the conditions at the cobpoint, as derived from the simulation of the shock propagation (WF1 and WF2) between t_c and the passage of the shock at *ISEE 3* (*vertical dot-dashed line*). Panels from top to bottom: BR, VR, the CMP angle (degrees) and the distance (AU) of the cobpoint to the Sun.

respect to the central meridian position (CMP). As can be seen, the differences in the cobpoint positions between the two cases are small. For low-energy particles, these differences will result in a small change in Q, because particles are injected from slightly different positions. For high-energy particles, which travel much faster than the shock, the differences between the two cobpoints become insignificant. Consequently, the fitting of the flux and anisotropy profiles in this event are practically independent of the topology assumed for the shock front. Nevertheless, the BR values (also in VR at the beginning) are different, because the WF2 shock is much wider than the WF1 shock. This would imply that any functional dependence that could appear between the injection rate and VR or BR, will depend on the modeling of the shock propagation. This is why it is very important to fix the initial conditions by using other spacecraft plasma data, as we did for the CM, E, and WS events; we will come back to this point in § 5.

4.2. Fitting the Flux and Anisotropy Profiles

As we discussed in the former section, we first fit the flux and anisotropy profiles in the upstream region of the 620–1000 keV channel, assuming that protons propagate along a
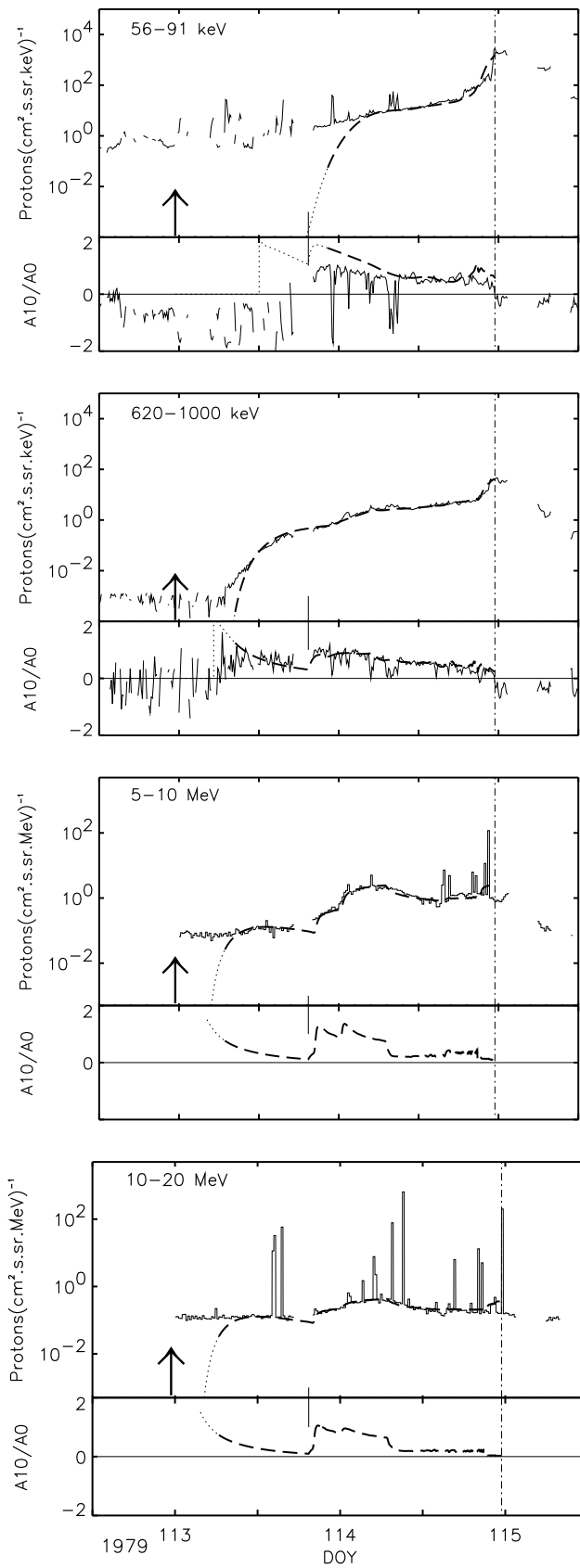
FIG. 3.—1979 April 24 event (CM event). Observed (*thin lines*) and fitted (*thick dashed lines*) flux and first-order anisotropy profiles. The thick arrow indicates the time of the solar activity, the dot-dashed vertical line indicates the passage of the shock, and the short solid vertical line shows t_c, the initial connecting time between the shock and the observer. The part of the profiles plotted as a dotted line (at the onset) is not physically meaningful; the background overwhelms the flux associated with the event.
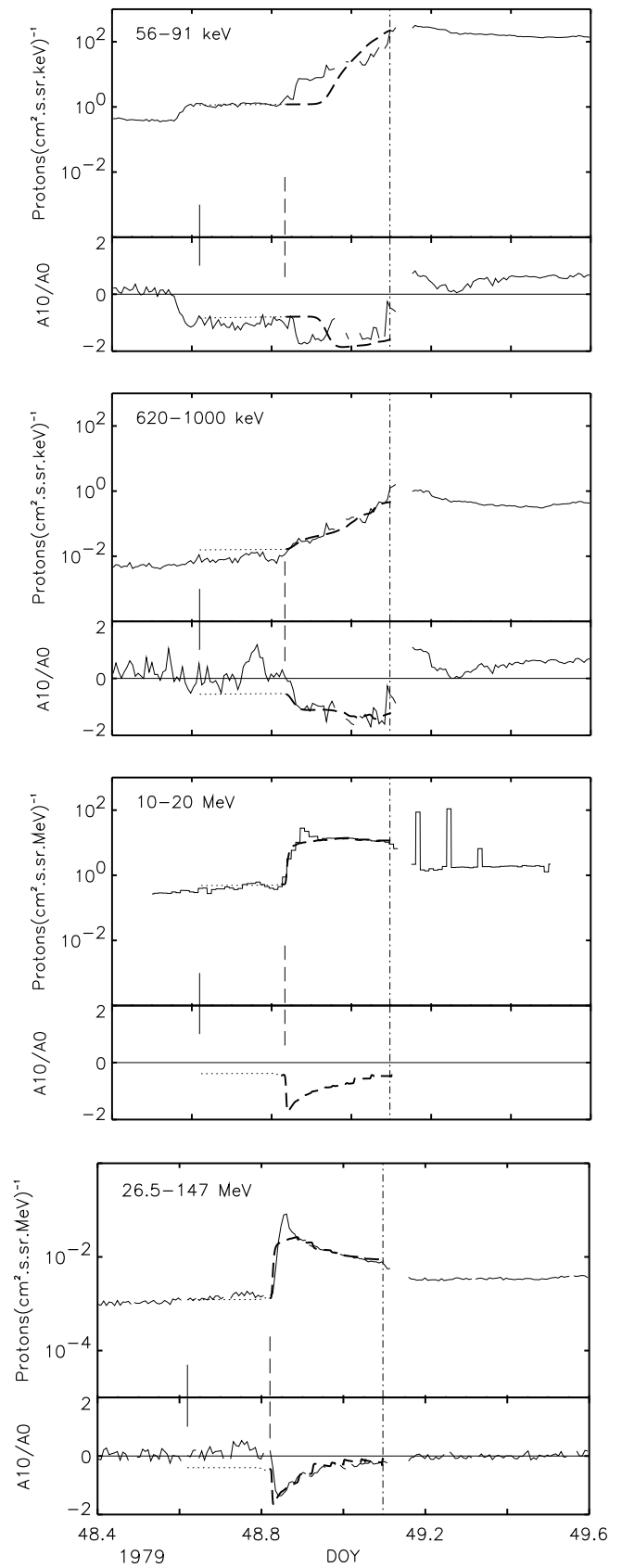
FIG. 4.—1979 February 18 event (E event). Lines are as in Fig. 3. Dashed vertical line marks the discontinuity commented on in the text.
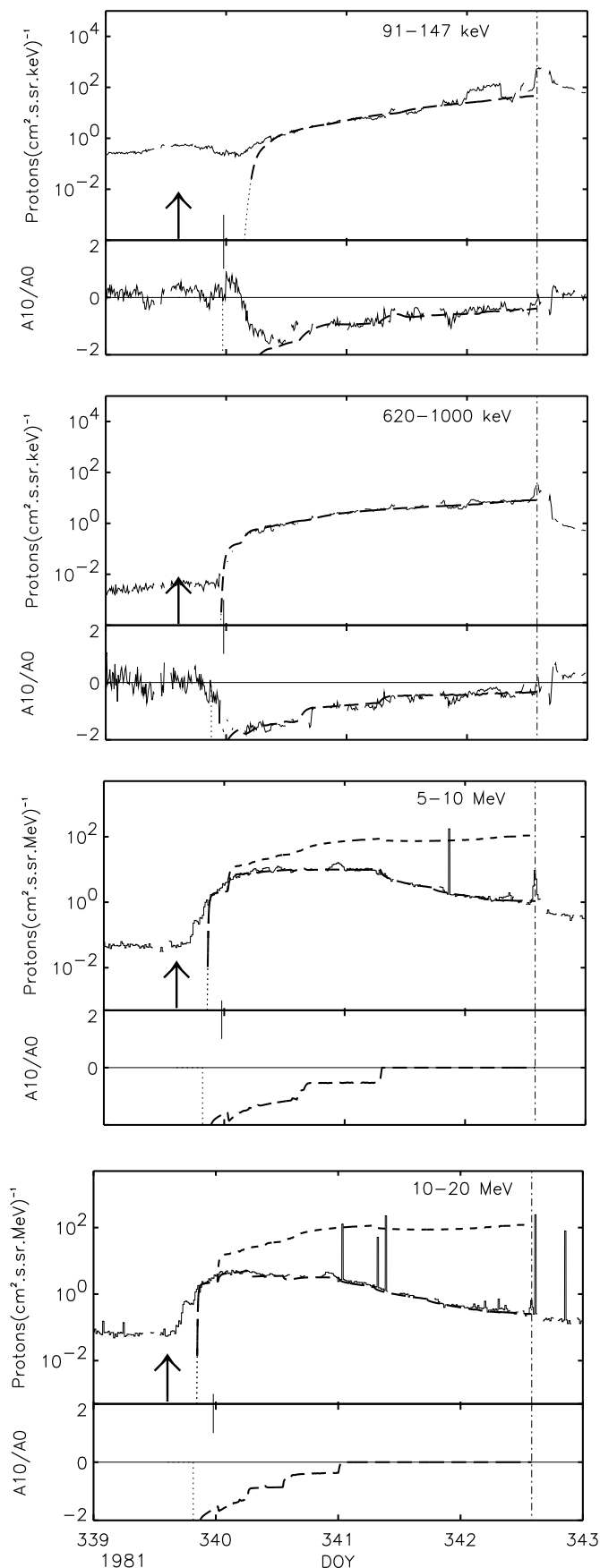
magnetic flux tube associated with the cobpoint. This yields the $\lambda_\parallel$ and G values for this energy. Then we use the spectral index γ to obtain the best fit for fluxes and anisotropies at lower energies. Figures 3, 4, and 5 show the fitting performed for the CM, E, and WS events at energies lower and higher than in He92 and He95, plus the fit at ~ 1 MeV from which the others at lower energies are derived (the total number of channels fitted is nine or ten for each event). Figure 6 shows the fitting performed for the WF event (taking $q = 1.4$); only the results for the WF1 shock are shown because the profiles for the WF2 shock are practically coincident.

The thick arrow in each panel indicates the time of the solar activity, the dot-dashed vertical line indicates the passage of the shock, and the short solid vertical line shows t_c, the initial connecting time between the shock and the observer. There is no arrow in Figure 4 (E event) because it should be out of the frame, more than 2 days to the left; the timescale for this event (~ 10 hr) is much shorter than for the other events modeled ($\gtrsim 40$ hr). The part of the profiles plotted as a dotted line (at the onset) is not physically meaningful; this part corresponds to the first particles arriving at the spacecraft, which cannot be seen because the background overwhelms the flux associated with the event. None of these figures display the lowest energy channel of *ISEE 3* (35–56 keV); at these energies there is always a large background population, which makes comparison with the observations rather difficult. Because of this contamination, the flux emerges from the background only a few hours before the shock passage. We will discuss this point when commenting on the WF event.

The CM event (Fig. 3) shows hardly any shock-accelerated protons for $E \gtrsim 10$ MeV, and the particle flux for $t < t_c$ results in a contribution that is below the background; at low energy, this initial component is more relevant. This event was associated with the disappearance of a quiescent filament (Sanahuja et al. 1983) and with a CME (Cane, Kahler, & Sheeley 1986), and did not show any signature of intense flaring activity (X-rays, type II emission, etc.). The lack of a satisfactory model for the formation of coronal shocks and its evolution to interplanetary (Cane 1997 and references therein), together with the location of the inner boundary of the shock model, obliges us to assume, in some cases, an injection of particles below this boundary and before t_c. The CM event requires a long-lasting injection, and it is clear that these are non–flare-accelerated particles.

Figure 4 shows the profiles for the E event. Because of a weak discontinuity several hours after t_c (Fig. 4, *short dashed line*), the model can only give an approximate fit of the profiles in this period, which in turn affects the overall upstream profile adjusted for the lowest energy channel. This is a consequence of trying to fit the profiles for several energy channels simultaneously; the fit can be improved by assuming slightly different solar wind conditions ahead of this point, or a different initial population in the magnetic flux tube to which the observer is connected. Nevertheless, we have preferred to keep the fits for all the events at the same level of complexity. Assuming the same conditions as at lower energies, for example, it is not possible to model the initial peak of the flux observed above 10 MeV.

Figure 5 shows the fits and observational profiles of flux and anisotropy for the WS event. The shock travels slowly, which implies a long-lasting injection of shock-accelerated
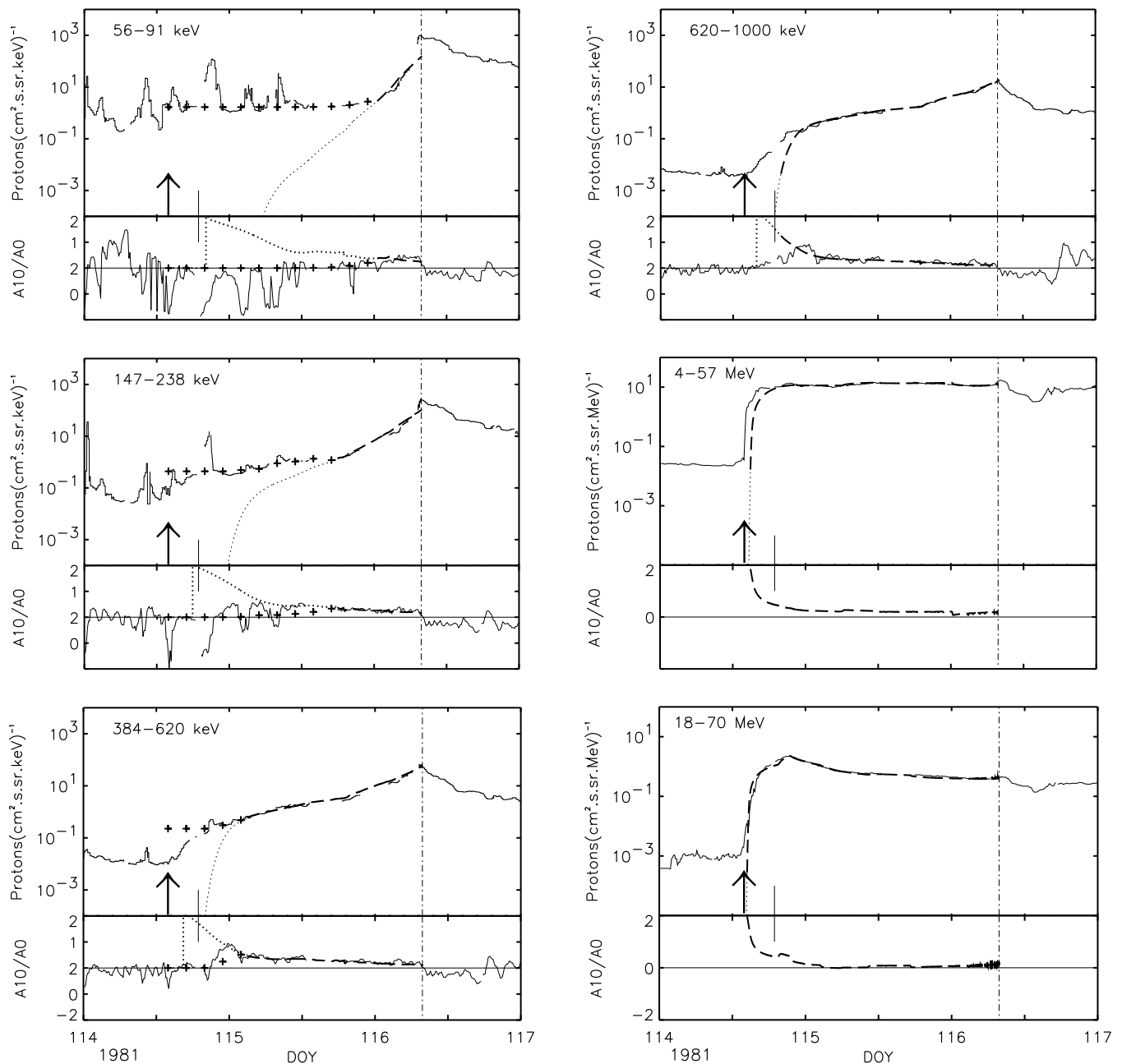
FIG. 6.—1981 April 26 event (WF event). Lines are as in Fig. 3. The line of crosses shows the flux profile obtained after including an isotropic population that simulates the preexisting background. Note the change in the anisotropy. The spikes at low energy correspond to the magnetospheric contributions (not simulated).

protons. The anisotropy decreases very slowly, and the fit does not require any region of increased magnetic turbulence ahead of the shock front. Looking at the evolution of the flux in the upstream region (i.e., ~ 30 hr ahead of the shock passage), we can see that the shock is still able to accelerate low-energy protons, but it has become very inefficient at high energy.

Figure 6 shows the profiles for the WF event. The flux and anisotropy profiles have been fitted assuming a constant injection of particles before t_c, as for the WS event, and a region of enhanced scattering upstream of the shock, characterized by a smaller mean free path, as for the CM event (see He92). We also assume that such a region has no effect on high-energy protons; although this is a reasonable

hypothesis (Kallenrode 1996), we cannot test it because the anisotropy profiles are not available (or derivable) at these energies. In this event, the IMF tubes were filled with an abundant low-energy population (a quasi-isotropic distribution) produced by a former event, and with spiky contributions of magnetospheric origin (highly anisotropic). These two populations mask the real anisotropy of the shock-accelerated population; below ~ 500 keV, the fits do not agree with the profiles observed until 10 or 20 hr (depending on the energy channel) before the shock passage. If we add to the fits a small isotropic population simulating this background (Fig. 6, *line of crosses*), the anisotropy is largely reduced, even to zero at the onset of the event, as the observations indicate. We cannot consistently introduce the

effect of the magnetospheric population that produces the antisunward flow (large negative anisotropies) when there is a good magnetic connection between *ISEE 3* and the bow shock of the Earth. Sanderson et al. (1981) present magnetospheric events of this type and discuss how they affect the values (and sign) of the anisotropy when riding upon larger energetic particle events. These contributions vanish as higher energies are considered.

The mean free path derived from the flux and anisotropy profiles observed in the 620–1000 keV channel for the CM and WS events are nearly identical to those found in He92 and He95. For the E event, we found $\lambda_{\parallel} = 1.3$ AU, and the fittings in the WF event yields $\lambda_{\parallel} = 0.1$ AU for the whole event in both WF cases. As commented on in § 2, the mean free path for other energies scales as R^{2-q}; all the values obtained are within the accepted range (i.e., Valdés-Galicia 1993). The inclusion of the solar wind effects at low energies leads to lower $\lambda_{\parallel}$ values than when those effects are not considered (see the discussion in Ru95). Furthermore, since we assume a $\lambda_{\parallel}(R)$ dependence in order to simultaneously fit the profiles for several energy channels, the mean free paths derived are not identical (although they are very similar) to those obtained using the focused-diffusion transport equation (Roelof 1969). These differences do not have any significant consequence for our analysis. The foreshock regions for the CM and WF events are characterized by $\lambda_{\parallel c}(\ll \lambda_{\parallel})$. The reduction of the integration grid allows us to take smaller mean free paths than the ones found in He92 for the fit (0.01 AU for the CM event, 0.02 AU for both WF cases), as well as thinner foreshock regions (0.04 and 0.2 AU, respectively). The smaller the grid, the more accurately the increase in the flux can be fitted at the shock passage.

4.3. The Injection Rate

Figure 7 displays the evolution of the injection rate of shock-accelerated protons, Q, for the four events. These values are derived directly from equation (1), after correcting for the cross-sectional area of the magnetic flux tube. The first point of each curve represents the injection at the connecting time, while the last point is the injection just before the shock passage at *ISEE 3*. The MHD model gives $t_c(E) > t_c(CM) > t_c(WS) \gtrsim t_c(WF)$. The longest elapsed time for the injection of protons corresponds to the WS event. The values of Q, computed through the dependence on $A(r)$, have been evaluated at the points of the grid given by the MHD simulation where protons are injected. Small jumps in Q caused by the discrete nature of $A(r)$ have been smoothed. The injection rate has an intrinsic radial dependence as r^{-2} (distance of the Sun to the cobpoint) through $A(r)$; thus, it should show a tendency to decrease with time as the shock moves away from the Sun. Nevertheless, it increases for CM and E events. The reason for this is that the evolution of Q depends basically on the quantity of particles available to be accelerated (not only from the solar wind but also from the particle population previously accelerated by the same shock or by other earlier events), the strength of the shock, and its ability to accelerate and to inject particles into the interplanetary medium.

The top panel of Figure 7 shows the evolution of Q for the 620–1000 keV channel. At lower energies, the values of Q are scaled according to the values of the spectral index γ discussed below. Curves labeled CM, WS, and E in the top panel of Figure 7 can be compared to the respective ones shown in Figure 8 of He95, showing that the evolution is
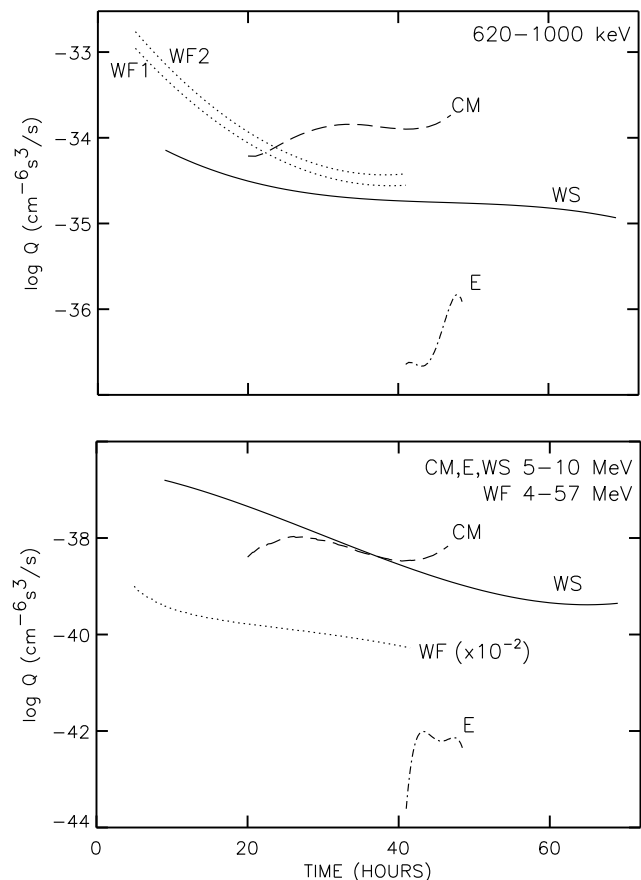

Fig. 7.—Evolution of the injection rate of shock-accelerated protons, Q, for the four events studied, at 620–1000 keV (*top panel*) and 5–10 MeV (*bottom panel*). The high-energy profile for the WF event displays the values for the 4–57 MeV channel. Each curve extends from t_c to the time of the shock passage by *ISEE 3*. The curves WF1 and WF2 shown in the top panel correspond to the WF event (see text).

essentially the same. This is a remarkable result, since the transport equation and the method used to integrate it are quite different; there are, however, small quantitative differences. Below 1 MeV, for example, the injection rate can be about twice as large as in He95. We attribute this difference to the combined effects of the solar wind convection and adiabatic deceleration; this is small at ∼1 MeV, but increasingly important at lower energies. Solar wind convection makes protons reach the observer sooner; therefore, in order to keep the flux high, a greater injection of fresh protons is required. Adiabatic deceleration demands large injections of protons because part of the flux decays to lower energies; this effect becomes important in impulsive injections. For a continuous strong injection from the shock, these effects are attenuated because protons travel shorter distances (as the shock is approaching the observer). Furthermore, the energy channels are populated in such a way that at the same distance and at the same time, the distribution of protons as a function of energy depends only on the spectrum of the injection, but not on the distance traveled (Lario et al. 1997). Therefore, the cumulative effect of deceleration becomes smaller. The top panel of Figure 7 shows two curves for the injection rate, corresponding to the evolution in the WF1 and WF2 cases. As discussed above, the differences between the injection rates derived are small at low energy and insignificant at high energy, and

they are derived from the position of the cobpoint at the front shock, which is very similar but not identical in both cases (Fig. 2, *two lower panels*).

The bottom panel of Figure 7 shows the evolution of Q at high energy: the 5–10 MeV channel for the E, CM, and WS events, and the 4–57 MeV channel for the WF event. At high energy, the particle fluxes have been fitted independently for each energy, because it is not possible to obtain results in agreement with the observations if we maintain the spectral index derived at low energy, even without knowing the anisotropy. For example, Figure 5 shows one extra curve for the two highest energy channels; these represent the flux profiles derived assuming the same spectral index as at low energy. At the shock passage, the discrepancy with respect to the observed flux is greater than 2 orders of magnitude, and it is practically independent of the $\lambda_\parallel$ assumed (even under scatter-free conditions); in fact, it is a consequence of the continuous injection of protons from the approaching shock. Therefore, the efficiency of the shock as particle accelerator decreases more rapidly when higher energies are considered; as Kallenrode (1996) pointed out, a high efficiency of particle acceleration at some MeV is not necessarily expected. Reames et al. (1997a) also suggest that in larger events, the efficiency for the acceleration of high-energy ions may decrease more rapidly than those at low energies as the shock expands outward from the Sun.

In broad outline, the evolution of Q at high energy (Fig. 7, *bottom panel*) is similar to the evolution at low energy; we will come back to this point in the next section. In the E event, the behavior of Q with respect to the energy is not the same at low and high energies; this may be due to the sudden connection, after the IMF discontinuity, to a magnetic flux tube containing a rich population of high-energy protons. The model can reproduce this feature by assuming a strong injection of protons coming from the shock after t_c. However, we suspect that this energetic population is associated with a 1B flare, located 10° east, erupting at 1439 UT on February 17 (Behannon, Burlaga, & Hewish 1991). In particular, the model cannot reproduce the flux peak observed above 10 MeV (which does not appear at lower energies). This contribution alters the Q values at this energy in this particular case. At low energy (<1.5 MeV), the evolution of the anisotropy after the discontinuity (day of year 48.8) removes the possibility of particle contamination from any other event: it is large and increases or keeps constant, then decreases sharply when the shock is approaching.

The spectra of the injection rates derived for the four events can be seen in Figure 8; the insets in the panels indicate the periods of time over which the injection rate has been averaged (from t_c to the passage of the shock). The energy assumed for each channel is the geometric mean of the interval; the error bars reflect the time dispersion, which means different injection rates at different energies for different intervals, and the change to differential flux units taken independently at each energy channel when computing Q. As can be seen, Q depends only slightly on the time considered, except for the WS event at high energy, and for the first interval of the WF event (these correspond to the WF1 case, and are nearly identical for the WF2 case). The first interval of the WF event is affected by the background population, which prevents a better fit to the profiles, without introducing further ad hoc assumptions. The
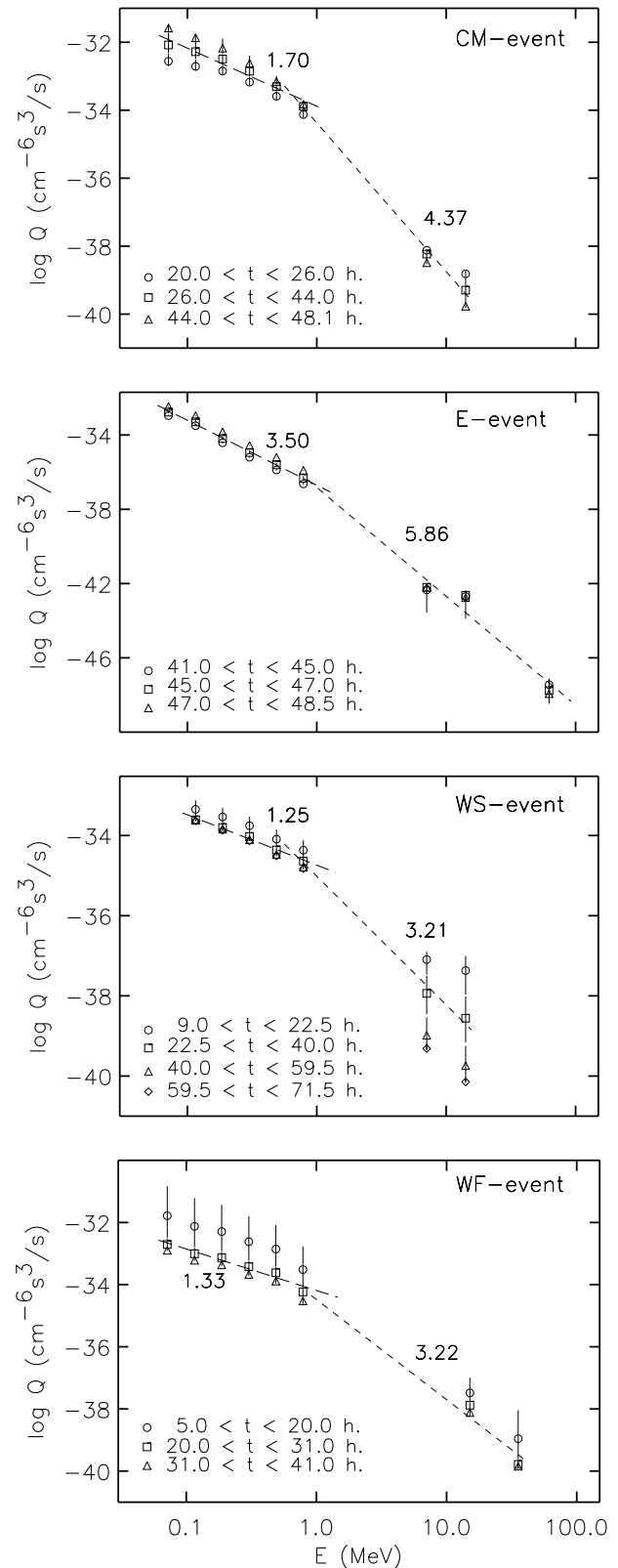

FIG. 8.—Spectra of the particle injection rate for the four events. Each point is the average value of Q over the period indicated in the inset, for each energy channel. The dashed line shows the fit to the points at low ($E < 2$ MeV) and high ($E > 1$ MeV) energy for the second period; the number is the corresponding spectral index, γ. The highest time value in each inset corresponds to the passage of the shock.

straight lines drawn in Figure 8 correspond to the best fit for the points of the second period plotted for each event, at low ($\lesssim 2$ MeV) and high ($\gtrsim 1$ MeV) energy, where the numbers are the respective spectral indices (absolute value of the slope). At low energy, the small dispersion guarantees that the values are representative of the whole set; the slope could change significantly at high energies, as indicated by the error bars. However, even taking into account this uncertainty, it is clear that the efficiency of the shock as an injector of accelerated protons decreases sharply above 2–5 MeV.

The low-energy spectral indexes can be compared with those given in Figure 8 of He92, and Figures 5 and 7 of He95. For the CM event, we assume that shock-accelerated particles start filling the flux tube of the cobpoint at t_c; this tube has already been populated by particles accelerated at the corona. Since equation (1) includes the solar wind effects, when the shock starts injecting particles into the tube, most of the solar-accelerated population is farther away than if the transport equation neglects the solar wind terms. Therefore, the shock starts filling a less populated flux tube, and consequently, higher injection rates are required to obtain a high and prolonged increase of the flux. The rigidity dependence assumed for the mean free path in the foreshock region ($\lambda_{\|c} \propto R^{-0.4}$) implies a more abundant population of ~ 1 MeV protons than that of ~ 100 keV protons. This dependence was also found by Beeck & Sanderson (1989), who analyzed several foreshock regions. Part of this energetic population feeds the lower energy levels, which does not happen if the transport equation does not consider the deceleration terms: in this latter case, the fitting of the profiles requires higher Q values at low energy, leading to a higher spectral index (a softer energy spectrum). In the WS event, the continuous injection of particles into the cobpoint magnetic flux tube makes the solar wind influence less perceptible; for that reason, the spectral index derived and that formerly estimated are similar. Once the magnetic connection is established, the E event shows a power-law spectrum with a slight softening when the shock is close to the observer. For this short event, the spectral

index is very sensitive to how the fit is performed.

The spectral indexes γ used in $G \propto E^{-\gamma}$ to obtain the fits of fluxes and anisotropies are given in Table 1. Note that the values displayed in Figure 8 correspond to the fit to the points of the second period plotted for each event, after computing the injection rate Q. The small differences between the values in Table 1 and those in Figure 8 do not affect the derived flux or anisotropy profiles. Figure 9 shows a representative example, the WS event in the energy channel 91–147 keV. The top and bottom panels display, respectively, the differences between the values of the flux and anisotropy profiles shown in Figure 6, and those calculated taking the slope displayed in Figure 8. When both profiles are coincident, the values shown in these panels should be zero; as can be seen, the solid line is close to zero. We have included in this figure two more lines in order to illustrate the sensitivity of the fit to the spectral index. These curves show the same magnitudes, but for spectral indexes equal to $\gamma + 0.25$ and $\gamma + 0.5$ (*dashed and dotted lines, respectively*); the first case produces a steady increase in the flux up to a factor of 1.5, while for the second the factor is 2.5.

We have seen in this section that a lower efficiency of the shock as a high-energy particle accelerator translates into a steepening of the energy spectrum of Q. This spectrum has usually been computed by measuring the intensity of particles at the moment of the shock passage, but not throughout the period during which the injection of particles from the shock lasts. Klecker, Scholler, & Hovestadt (1983) studied the variations of intensity, energy spectra, and composition of ions in the energy range 0.3–20 MeV for an event observed by *ISEE 3* on 1978 September 29. About 2 hr before the shock passage, the spectrum of the differential flux of protons (their Fig. 6) has a slope of 1.9 for $E \lesssim 1$ MeV; the spectrum above this energy softens as the slope changes to 4.1. Nevertheless, this is not a clear example, because the energy range covered only extends up to 2 MeV, and they were implicitly assuming that the transport of protons during these 2 hr had not modified the spectrum.

Reames et al. (1997a) reported spectral invariance during a 3 day period for a gradual particle event on 1995 October 20, starting almost 1 day before the shock arrival. Their

TABLE 1

THE SPECTRAL INDEX

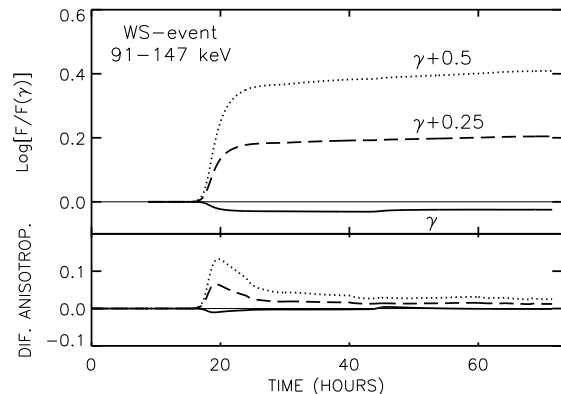| Time (hr)	γ
CM event	
$t_c \leq t < 26$	1.51
$26 \leq t < 44$	1.71
$t \geq 44$	2.21
E event	
$t_c \leq t < 45$	3.61
$45 \leq t < 47$	3.47
$t \geq 47$	3.37
WS event	
$t_c \leq t < 40$	1.21
$t \geq 40$	1.41
WF event	
$t_c \leq t < 20$	1.70
$20 \leq t < 31$	1.28
$t \geq 31$	1.50

FIG. 9.—1981 December 8 (WS) event, ~ 100 keV channel. Differences between the flux and anisotropy profiles shown in Fig. 5 and those calculated assuming that the spectral index estimated in Fig. 8 applies to the whole event (*solid line*). The top panel shows the logarithm of the flux ratio; bottom panel shows the subtraction between both anisotropies. The other two curves in each panel show the same magnitudes, but assuming two arbitrary slopes, as labeled.

Figure 7 shows that the slope of the proton flux spectrum is between 2.5 and 3.1; there is a slight softening above 10 MeV. We think that it is not immediately apparent to relate these values to the slope of our distribution function source term, Q, either because of the possible presence of a turbulent foreshock region ahead the shock (as suggested by the different evolution of fluxes immediately ahead of the shock; see their Fig. 6), or because of the transport effects of the IMF on the particle population, especially when the shock is farther away from the observer. Reames, Kahler, & Ng (1997b) point out that the slope of the differential flux spectrum in the invariant region largely varies among different events (between 1.7 and 4.1), with many spectra steepening at high energy. If the downstream population is a reservoir population for later shock acceleration, we should expect a softer spectrum at low energy immediately ahead of the shock, because the acceleration process is more efficient at low energy than at high energy. Nevertheless, in the upstream region the shock-accelerated particles can interact with the magnetic field, thereby further modifying the spectrum. Thus, the spectrum measured in the upstream region results from competition among three factors: the initial spectrum of the seed population, the efficiency of the shock as a particle accelerator, and the modulation due to the IMF. These factors, as well as their energy dependence, can be different from event to event. They could yield a variety of spectra, softening in different degrees and at different energies.

5. EVOLUTION AND FEATURES OF THE INJECTION RATE

5.1. Evolution of the Injection Rate of Shock-Accelerated Particles

This is the first time that the quantitative evolution of the injection rate and its spectrum for long-lasting energetic particle events have been modeled at energies higher than 2 MeV; He95 presented similar results at low energy, although the evolution of Q was only schematically described because the transport equation and the hypotheses assumed did not permit a link of the fits performed at different energies. The evolution of Q for the WS and WF events (Fig. 7) shows that these shocks inject more particles into the interplanetary medium when they are close to the Sun than when they are approaching a distance of 1 AU. The injection rate decreases more than 1 order of magnitude at all energies in both events (in some cases even up to 2.5). This decreasing efficiency of the shock as a particle accelerator results from the combination of two effects: the evolution of the cobpoint along its front (moving clockwise, as seen from the Sun), and the expansion of the shock (weakening its MHD strength). When a west shock is still close to the Sun, its cobpoint is located in the central part of the front, where the shock is stronger (the highest VR values). However, when this shock is near 1 AU, the cobpoint has slipped $\sim 50°$ away from the central part of the front to the right flank (which means lower VR values).

In contrast to what happens in the west events, the injection rate at low energy increases with time in the CM and E events. The evolution of VR also shows a monotonic increase in both cases. The magnetic compression increases monotonically in the E event, while in the CM event it grows until the cobpoint reaches 0.4 AU, and then remains stable and high (~ 3.5) for the rest of the upstream event. It seems that for the CM event, Q increases until BR reaches

its maximum value (at $t \sim 24$ hr). This behavior reflects the approach of the cobpoint to the nose of the shock, and thus the increase in Q. At high energy, for the same event, Q decreases slightly, showing a weakening of the shock as a high-energy particle accelerator. Nevertheless, we cannot attach much significance to this conclusion, since the flux at 10 MeV scarcely stands out over the background.

It is clear from Figure 8 that the Q spectrum does not extend smoothly from low energies (~ 50 keV) to high energies (100 MeV or, as a more conservative limit, 50 MeV) in any of the four events modeled. From these limited results (because of the small number of points and events), we cannot conclude that the diffusion mechanism does not work above ~ 2 MeV, or whether the shock-acceleration processes have not yet reached the steady state regime (Forman & Webb 1985). To obtain more accurate results at high energy demands more sophisticated observations (better spatial and temporal resolution), which should allow us to apply the same procedure at high energy as at low energy to fit the flux and anisotropy profiles.

As can be seen in Figure 7, the injection rate at low energy decreases more slowly in the WS event than in the WF event. However, the opposite happens at high energy; the WS event decreases by 2 orders of magnitude, while the WF event decreases by 1. Both events have a similar heliolongitude, and the magnetic compression shows a similar evolution at the cobpoint. The most significant differences are their respective durations (or, equivalently, the velocity of propagation of the shock), and the evolution of the velocity compression, VR, at the cobpoint. VR is about twice as large for the WF event as for the WS event. Furthermore, the WS event develops over a normal isotropic background of protons, and it is not necessary to assume a high-scattering region at any energy, while the WF event grows over a former particle event, and its simulation requires a foreshock turbulent region active at low energy. In addition to the influence of the foreshock region, the presence of a seed population also favors the acceleration of particles (Tan et al. 1989). The combined influence of both factors may explain the differences between the injection rates of the two events, leading to higher Q values in the WF event.

We have already mentioned that the injection of particles before t_c constitutes the component of those particles accelerated close to the corona. The temporal evolution of this injection is given by a constant injection (west events), by a Reid-Axford profile (CM event), or is not considered (E event). This is a useful way to represent an injection of particles from the corona, which allows us to include the effects of a possible coronal shock propagating close to the Sun, or the existence of an impulsive injection of particles. The effects of this injection close to the corona frequently appear in the literature; for example, when Cane (1996) defines "eruption" or "CME/eruptive flare." The current state of shock modeling does not allow us to simulate this contribution within the global scenario of our combined shock-particle model. In the west events, we cannot discern the exact value of t_c because the inner boundary of the MHD model does not permit us to go closer than 18 $R_\odot$. For such magnetically well-connected events, an observer is connected to the particle source from the time of the occurrence of the solar activity that triggers the event. At that time, the newly formed shock accelerates large quantities of particles because it propagates in a dense medium with strong embedded fields. Although a realistic model for

this scenario has not yet been proposed (Kahler 1992), the best approach was taken by Lee & Ryan (1986), who investigated the acceleration and propagation of particles at an expanding coronal shock, presenting different time profiles at 1 AU. Nevertheless, as they commented, these profiles cannot be directly compared with the observations. For our purposes, a more serious flaw of this model is that it neglects the role of the magnetic field and uses a diffusive equation. Another example of the existence of a strong component of particles accelerated close to the Sun is the WF event, which shows an impulsive and a gradual component (§ 3). In particular, the Fe/O ratio is high until ∼5 hr after the onset of the event, which coincides with the connecting time, t_c, derived from the MHD simulation. The first phase of the injection is closely associated with type III bursts, and it has also been inferred indirectly from the absence of an associated coronal shock in different events (Cane & Reames 1990). On the other hand, the WS event does not show any change in chemical abundances (Kahler et al. 1986), which suggests a unique agent for the particle acceleration. Kahler, Reames, & Sheeley (1990) examined several injection profiles (for 175 MeV protons) between 2 and 10 $R_\odot$, suggesting that these particles are accelerated in shocks driven by CMEs. Unfortunately, there are few west events for which the impulsive and gradual components have been reasonably well identified; their analysis would be very helpful to understanding the evolution of the shocks from the corona to the inner interplanetary medium.

5.2. Dependence of Q on the MHD Strength of the Shock

The injection rate can now be evaluated during the evolution of the event, since the effect of the interplanetary transport has been removed (at least to a first approximation) by making allowances for the boundary conditions of the model and the size of the MHD grid. Figures 10, 11, and 12 show the evolution of Q as a function of VR, BR, and θ_{Bn} at the cobpoint for the four events modeled. The two upper panels in Figure 10 display the evolution of Q for the CM and E events (*top*) and the WS and WF events (*middle*) at low energy (two channels); the two curves that appear at each energy for the WF event represent the fittings for the WF1 and WF2 cases. The lower panel shows high energy (one energy for each event). Each point represents a time step of the numerical integration at which particle injection occurs. The thin arrows in the top two panels indicate the direction of increasing time. In the top panel, the points to the left correspond to MHD conditions of the shock when it is still close to the Sun, and the points to the right indicate when the shock is close to 1 AU. The opposite is true for the middle panel; in the bottom panel each set tracks the evolution of the corresponding event in the upper panels. This time evolution is a straightforward consequence of the evolution of Q discussed above. The dashed line shows the result of a simple linear regression to each set of points (black dots); when the coefficient of the regression, ξ, is less than 0.75, the values are represented by open circles (only the E event at high energy). The statistical analysis yields the following values for the coefficient ξ at ∼100 keV, ∼1 MeV, and $\gtrsim$4 MeV, respectively: CM event, 0.88, 0.86, and 0.94; E event, 0.75, 0.75, and 0.52; WS event, 0.76, 0.94, and 0.98; WF1 event, 0.99, 0.94, and 0.98; and WF2 event, 0.98, 0.99, and 0.99. For the intermediate energy channels not represented in Figure 10, ξ is around the corresponding values given here. The ξ values found for the E event are
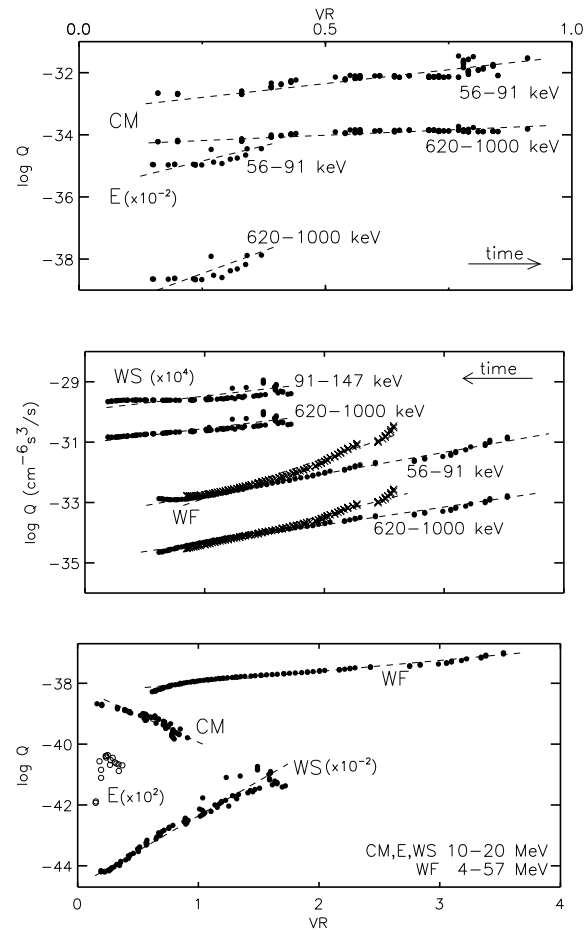

FIG. 10.—Representative examples of the dependence of the injection rate, Q, on the normalized velocity ratio, VR. *Top panel*: low-energy fits for the CM and E events. *Middle panel*: low-energy fits for the WS and WF events (filled circles in the WF event represent the WF1 case, crosses represent the WF2 case). *Bottom panel*: high-energy fits for the four events. The top scale of VR only applies to the top panel. Straight dashed lines follow a log $Q \propto$ VR dependence. Open circles represent the cases for which the linear regression has a correlation coefficient lower than 0.76. The arrows indicate increasing time in each case (see text).

lower because this event develops rapidly, less than half a day between t_c and the passage of the shock, which limits the evolution of VR.

Table 2 gives the coefficients found for the relation log $Q = \log Q_0 + k$VR, and the e-folding, $VR_c = \log e/k$, for each event at low energy. The values derived from these lineal regressions have physical meaning only for the range
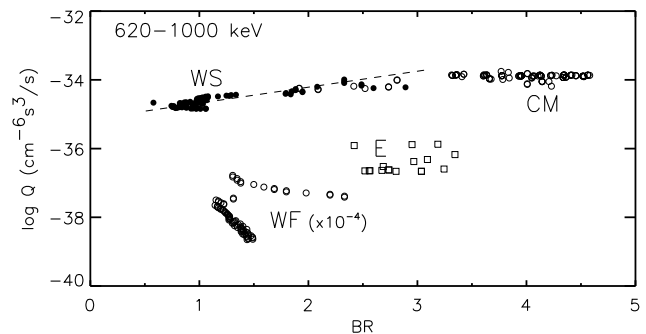

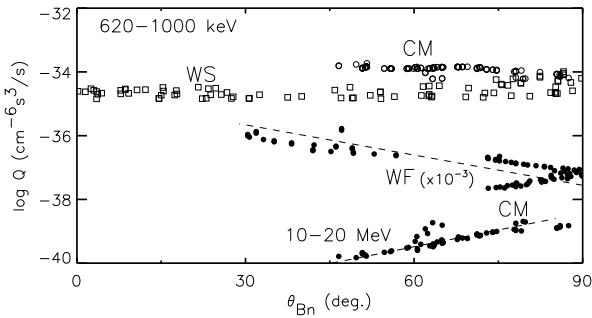FIG. 11.—Dependence of the injection rate, Q, on the magnetic field ratio, BR. Plots are as in Fig. 10.

FIG. 12.—Dependence of the injection rate, Q, on the angle θ_{Bn}. Plots are as in Fig. 10. The points associated with the E events have not been included, for clarity.

of VR values found; $VR \geq 0.10$ is the lower limit from which the injection has been considered active. Thus, Q_0 should be understood as the injection rate of accelerated particles when the shock-acceleration process starts. For the WF event, for example, VR decreases from 3 or 4 to 1 (the shock is strong close to the Sun, but much weaker at 1 AU), which represents a reduction of Q by 2 orders of magnitude at low energy. The values of these coefficients at high energy must be taken with caution, because of the uncertainty involved in their derivation; we include them in Table 2 so that they can be compared to the coefficients at low energy. Lario et al. (1995b) have modeled the evolution of the flux at ~ 1 MeV for four particle events, assuming this dependence for the injection rate of shock-accelerated particles, and assuming an average MHD shock obtained from a set of shocks producing large gradual particle events. In spite of these drastic simplifications, the fits obtained are surprisingly good. The different slopes found for the two cases considered in the WF event reflect the different evolution of VR; thus, to correctly quantify the dependence of Q

TABLE 2

Coefficients for the Relation $\log Q = \log Q_0 + kVR$
(for $VR > 0.10$)

Energy	Q_0 (cm^{-6} s^3 s^{-1})	k	VR_c
	CM event		
90 keV	5.3×10^{-34}	1.52	0.29
1 MeV	4.4×10^{-35}	0.69	0.63
~ 15 MeV	6.8×10^{-39}	-1.76	-0.25
	E event		
90 keV	3.6×10^{-35}	4.29	0.10
1 MeV	1.2×10^{-38}	5.84	0.07
	WS event		
90 keV	1.4×10^{-34}	0.40	1.08
1 MeV	1.0×10^{-35}	0.46	0.94
~ 15 MeV	2.0×10^{-41}	2.40	0.18
	WF Event: WF1		
90 keV	1.8×10^{-34}	0.68	0.64
1 MeV	1.2×10^{-35}	0.59	0.74
~ 15 MeV	4.5×10^{-39}	0.36	1.19
	WF event: WF2		
90 keV	4.2×10^{-35}	1.26	0.34
1 MeV	3.2×10^{-36}	1.04	0.42
~ 15 MeV	1.5×10^{-39}	0.72	0.60

on VR it is necessary that the MHD code model reproduces the real evolution of the shock as best as possible.

We have proceeded with BR and θ_{Bn} in the same way as with VR. Figures 11 and 12 show the results, which are completely different from those obtained for VR (we only present one energy channel for each event). The linear regression performed for the magnetic field compression ratio only gives significant results in the WS event ($\xi = 0.83$). Nevertheless, we cannot extract any clear conclusion from these data because most of the points group around BR ~ 1, which is a typical value of BR during most of the event (except at the onset). Thus, if there is any dependence of Q on BR, it is too weak to be detected at this stage of our modeling. The same conclusion holds for other energies of the same event, and for the WF event. The argument given in the preceding paragraph for the E event is valid here (and is also valid for θ_{Bn}). The CM event is a different case, because BR is high about 1 day after the onset of the event, and it remains high until the passage of the shock. But it also shows important fluctuations (Fig. 3 of He95), while the injection rate varies slowly. Looking at the points associated with this event (Fig. 11), the injection rate does not appear to depend on BR, or else the dependence is too weak for our model to discern it.

A similar conclusion can be drawn for the dependence of Q on θ_{Bn} (Fig. 12); in this case, the dispersion of the values is even larger than for BR. The E event has not been plotted, for clarity; all points cluster around 82° because the E shock is quasi-perpendicular. The points plotted in this figure do not reflect any time sequence (as in Fig. 10); ξ is lower than 0.20 for the WF and WS events. In both events, the cobpoint stays for a long time in a region of the respective shocks where the magnetic field presents a low downstream/upstream ratio (BR ~ 1). To derive θ_{Bn}, we apply the coplanarity theorem, following Chao & Hsieh (1984), which implies a number of interpolations upstream and downstream of the shock front as a result of the discrete nature of the MHD grid. When the magnetic compression is low, the oscillations of the components of the magnetic field (upstream and downstream) yield important variations in the values derived for θ_{Bn} (Balogh et al. 1995), even if the front is perfectly identified by the jump of the hydrodynamic variables (velocity or density). In short, we cannot draw any conclusion about the functional dependence of Q on θ_{Bn}, because of the uncertainties in the determination. The only significant result corresponds to the CM event at high energy; ξ is 0.84 and 0.87, respectively, for the 5–10 MeV and 10–20 MeV channels (0.59 for the 620–1000 keV channel). In this case, Q decreases with θ_{Bn} (this shock evolves from quasi-perpendicular to quasi-parallel conditions), which means that the efficiency of the shock as an accelerator diminishes when the condition of perpendicularity is lost. This evolution seems to indicate that the shock-drift process works efficiently at high energy, but that at low energy the shock-diffusion mechanism is more efficient.

It is possible to synthesize the flux and anisotropy profiles that should be observed by another spacecraft, provided that it is magnetically connected with the front of the shock. The evolution of the cobpoint associated with this second spacecraft can be easily evaluated from the simulation of the shock, and therefore it is possible to derive the values of the MHD variables at that point. Accepting that there is a dependence of the injection rate of shock-accelerated par-

ticles on these variables at the cobpoint (VR in our case), it is straightforward to build up the flux and anisotropy profiles that this second spacecraft would observe. The most favorable situation for such a prediction appears when the cobpoint associated with the second spacecraft moves through the region of the shock front already covered by the cobpoint of the spacecraft already simulated, or nearby. The worst situation appears when the cobpoint is at the wings of the shock, or, for the East events, where the evolution of Q only extends for a short period. Among the four events studied, only the CM event offers an adequate scenario; Figure 5 of Sanahuja et al. (1983) shows the position of *Helios 1* and *Helios 2* with respect to the shock and *ISEE 3*, and Figure 1 of He92 shows the evolution of the shock modeled. The cobpoint of *Helios 2* moves in a region of the shock that is later scanned by the cobpoint of *ISEE 3*; therefore, it is easy to derive the values of Q associated with the cobpoint of *Helios 2* taking into account the VR values given by the MHD simulation. Figure 13 shows the observed flux profiles at low energy for two similar channels of *Helios 2* and *ISEE 3*. The dashed lines show the flux profile fitted to *ISEE 3* flux data (the third energy channel, not shown in Fig. 3), as described in § 4, and the flux build-up for *Helios 2*; we have assumed the same mean free path for the particles at the same time. As can be seen, the observed and synthesized profiles fit closely. We can proceed in the same way at high energy, particularly with the 4–6 MeV channel of *Helios 2*, and we can obtain similar good fits. Unfortunately, for this energy range there are only two or three observational points in the upstream region of *Helios 2* (I. Richardson 1996, private communication; see also Fig. 2 of Richardson 1997), therefore, the result at high energy is not especially relevant, since there are a wide range of power laws that can yield good fits.

The model also predicts that *Helios 1* should observe a large low-energy particle event, because it is magnetically connected to the central part of the shock, and as the shock propagates the cobpoint slips towards its right wing. But the observations reveal nothing (Sanahuja et al. 1983). Burlaga, Behannon, & Klein (1987) describe the scenario of this event in detail (see their Figs. 8–12); there is a corotating stream perturbation progressing counterclockwise that modifies the conditions of the ambient solar wind and the IMF topology assumed by the model. The front of such a discontinuity modifies the magnetic connection between the
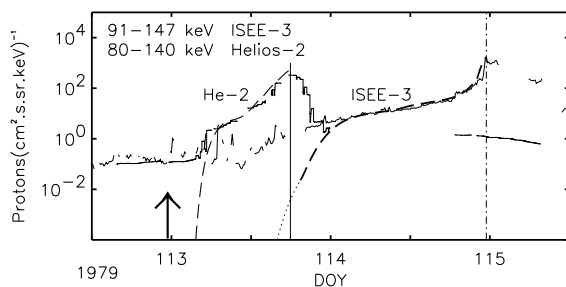
spacecraft and the front of the shock, and most probably prevents the arrival of the low-energy particles accelerated by the shock. It is also possible that the front of the stream interacts with the right wing of the progressing shock, preventing the formation there of a true shock front. Watanabe & Kakinuma (1984) depict such a scenario from radio-scintillation observations. The MHD code for the shock is not prepared to take into account a highly perturbed solar wind; thus, we cannot describe what really happens in the right wing of the shock. Nevertheless, the presence of this stream does not modify our conclusions about the injection rate of particles for this event, since *Helios 2* and *ISEE 3* are not affected by the presence of this stream until after the passage of the shock by *ISEE 3*.

An interesting point to note is the dependence of the injection rate on the radial distance to the Sun, r, and on the angular distance to the nose of the shock, the azimuthal distance (i.e., Reames et al. 1996 and references therein). As the position of the cobpoint and the value of Q are known throughout the event, it is easy to fit the evolution of Q as a function of r. Assuming a power law like $Q \propto r^\alpha$, the exponent α should characterize the evolution of the injection rate. For the CM event, the values of α found vary between 2.0 (56–91 keV) and 0.7 (620–1000 keV); the difference in the exponents reflects the fact that Q increases with the distance and the spectrum weakens as the shock approaches the observer. At high energy, Q decreases with distance ($\alpha = -0.8$ at 5–10 MeV and $\alpha = -2.4$ at 10–20 MeV), a behavior also expected from the weakening of the shock. For the two west events, α ranges between -4.8 and -0.6 (depending on the energy); Q decreases with distance, reflecting the weakening of the shock and the movement of the cobpoint away from its nose. Another possibility, explored by Kallenrode (1996), is to assume an exponential decrease for Q along the shock front, and to derive the e-folding angle, Φ, for each event. At low energy, the values found for Φ range between 9° and 58° for the four events; large values mean that the injection rate is less dependent on the azimuthal distance. At high energy, the fits yield negative values for the CM event, and angles between 7° and 34° for the west events. According to these results, any possible azimuthal dependence of Q along the shock front should be different at different energies, and not necessarily constant during the evolution of the event. The injection rate may not be completely represented by a radial or an azimuthal dependence alone; Kallenrode (1997a) refers to similar situations. We must bear in mind that the injection rate depends not only on the movement of the cobpoint due to the expansion of the shock, but also on the MHD conditions for the shock acceleration and injection of particles at this point, and on the shape of the shock, which changes during its interplanetary journey.

5.3. The Influence of Corotation

The scenario adopted for modeling the four particle events assumes a stable solar wind regime, and thus an Archimedial structure for the IMF upstream of the shock. Consistently, we can only interpret the quantitative evolution of Q correctly in terms of the evolution of the shock, if the topology of the upstream IMF does not change significantly during the event. But even under such favorable conditions, the corotation of the magnetic field tubes (and of the particle population filling them) could affect the conclusions. This "corotation effect" is a consequence of the solar

FIG. 13.—CM event. Low-energy flux profile derived for *Helios 2*, assuming log $Q \propto$ VR. Thin lines show the flux profiles measured by *ISEE 3* and *Helios 2*. Thick dashed line shows the fit for *ISEE 3* derived from the fit performed at ~ 1 MeV. The thin dashed line shows the flux profile synthesized for *Helios 2*, under the assumptions commented on in the text. Vertical lines represent the shock passage, and the arrow indicates the time of the filament disappearance.

rotation: while the shock is propagating out from the Sun, the background medium is rotating westward at a rate of ~13°6 per day. An Earth-orbiting observer located at ~1 AU will scan different magnetic flux tubes, filled with shock-accelerated protons injected from eastern regions of the front (to the right, as seen from the Sun). For that reason, corotation might lead to changes in the flux as a result of the spatial evolution of the tubes, and the more slowly the shock propagates, the more flux tubes will sweep the space-craft before the shock arrival.

Until now, the observer was considered to be in a unique flux tube, which, as the shock expanded, remained connected to different regions of the shock front (cobpoint). The particles injected from the cobpoint filled the same magnetic flux tube. The inclusion of the corotation effect involves the simulation of different flux tubes, each one connected to different parts of the shock. Therefore, it is necessary to fill the several flux tubes that, one after the other, will sweep across the observer, and to study the temporal dependence of the particle population in each flux tube. A direct consequence of including corotation in the model is that the CPU time needed to produce a fit is greatly increased, because it is necessary to include the contribution to the flux coming from different IMF tubes. It is possible to analyze the influence of corotation, assuming a functional dependence of the injection rate with respect to the position of the cobpoint along the shock front. There have been qualitative suggestions for such dependence (Reinhard et al. 1983; Sarris, Decker, & Krimigis 1985, among others), but up to now, only Kallenrode & Wibberenz (1997) have explicitly taken it into account, assuming that the flux intensity decays exponentially from the central part of the shock toward its flanks. In our case, assuming that $\log Q \propto VR$, we are implicitly considering the influence of the angular distance from the central part of the shock, as well as the temporal evolution due to its propagation.

The thick solid line in Figure 14 shows the difference between the flux profile obtained for the WF event (at ~1 MeV, Fig. 6) and the profile that results after including the corotation effect, assuming $\log Q \propto VR$ (for the WF2 case). We have computed the evolution of the 36 magnetic flux tubes (0°33 wide) to the right of the formerly original tube. We have replaced the contribution of each tube by the contribution of the next one to the right when the magnetic connection (the cobpoint) changes due to corotation. The
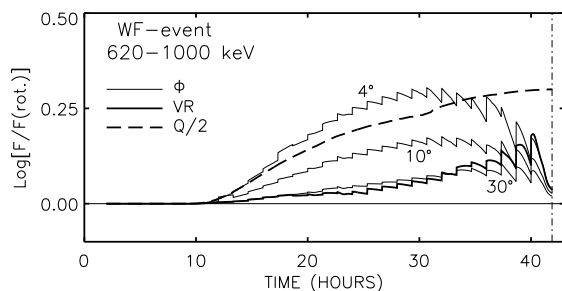
global influence of corotation is small, in spite of the shock taking nearly two days to reach 1 AU. It is also clear, however, that for certain periods, corotation could modify the injection rate derived by a factor of 1.4 at the maximum, depending on the geometry of the scenario (position of the observer with respect to the shock) and the velocity of propagation (strength) of the shock. The thick dashed line shows the same difference computed assuming that the injection rate taken is one-half the value needed to fit the profiles in Figure 6 (the WF1 case yields the same conclusion). The net effect of corotation, in this case, is to underestimate Q by a factor of 0.5 between 18 and 25 hr after the onset of the event. These differences are smaller for the E and CM events, and similar for the WS event; in the latter case, the shock propagates more slowly than in the other events, but Q and VR also vary slowly.

The jumps that appear in the curves of Figure 14 correspond to changes from one flux tube to another. These discontinuities can be smoothed using a finer grid of tubes, but we have preferred to keep the same grid used to compute all the flux and anisotropy profiles, since increasing the number of tubes implies modifying the MHD grid used for the simulation of the shock. We have not explored the importance of this effect at distances greater than 1.2 AU, since it is beyond the present possibilities of our code. The effect of corotation should be kept in mind, since it might be important when the shock velocity is low, when the observer has a proper motion with respect to the shock, or when the injection rate of shock-accelerated particles is strongly dependent along the shock front. Kallenrode & Wibberenz (1997) discuss the importance of corotation in similar terms for shocks with increasing or decreasing efficiency with radial distance, also depending on the observer's position with respect to the central part of the shock.

Kallenrode (1996) suggests that the flux intensity decays exponentially from the central part of the shock toward its flanks. The e-folding decay is characterized by an angle $\Phi = 10°$. This is an interesting result, but it must be taken with caution, because the set analyzed is small and it encompasses values between 4° and 180°; consequently, the coefficients of correlation found are not significant (see discussion in Kallenrode 1996). Nevertheless, it is reasonable to explore the influence of such a dependence in the corotation effect. We can assume that Q behaves like the intensity, having its highest value at the nose of the shock, with a symmetric decay toward the flanks. Note that this angular dependence is not directly related to that suggested for the intensity, and there is no clear evidence of the symmetry of the decay. Figure 14 includes three curves (thin lines) showing the differences between the profile obtained in Figure 6 and those obtained assuming $\Phi = 4°$, 10°, and 30°, respectively. The differences are large for the lowest value, and they are practically independent on Φ above 30°. This is an expected result, since for a given shock an ad hoc azimuthal evolution of Q (i.e., an appropriate Φ) could mimic the evolution of Q due to the shock expansion. As can be seen in this figure, the effect of the corotation in this event can be reasonably modeled assuming $\Phi = 30°$, but when the WF1 case is considered, $\Phi = 10°$ is a more appropriate value (the thick VR line tracks closer to the 10° curve, instead of the 30° curve). The reason is clear: the WF2 shock has a wider front than the WF1 one, whereas the Q-values derived from the fittings of flux and anisotropy are very similar; consequently, the e-folding angle must be

FIG. 14.—1981 April 26 (WF) event, ~1 MeV channel, showing the influence of corotation. *Thick line*: difference between the flux calculated without corotation and the resulting flux that includes this effect. *Thick dashed line*: the same difference, but assuming an injection rate equal to half that obtained without considering corotation. *Thin lines*: differences found assuming an exponential decay for Q, with $\Phi = 4°$, 10°, and 30°, as labeled.

larger for the wide front shock than for the narrow one. Therefore, it is not clear that assuming that all shocks have a semicircular shape could result in a characteristic e-folding angle representative of a large fraction of the events.

6. CONCLUSIONS

We have presented an improved version of a numerical code for studying energetic particle events associated with interplanetary shocks. The major improvement over the former version of the model is in the transport equation describing the particle propagation along the IMF, which now includes the effects of solar wind convection and adiabatic deceleration. In order to minimize the parameters of the model, we have assumed a dependence of the injection rate ($\propto E^{-\gamma}$) and of the mean free path ($\propto R^{2-q}$) on the energy of the particles. In this way, by fitting the observed particle flux and anisotropy profiles at only one energy channel, we obtain simultaneously all the other low-energy channels, reducing the arbitrariness of fitting each energy channel on its own. We have used this model to reproduce the observed flux and first-order anisotropy profiles for four particle events, extending the energy range between ∼50 keV and 100 MeV. The results have been compared with former results (He95), explaining the differences and/or the good agreement between them. From the fits performed for each event, we have been able to derive the injection rate of shock-accelerated particles and its energy spectrum at the cobpoint, while the shock is propagating from near the Sun to 1 AU. We have quantified this injection and have found that the efficiency of the shock as a particle accelerator decreases more rapidly above ∼2 MeV than at lower energies.

We have related the evolution of the injection rate to the evolution of the MHD strength of the shock at the cobpoint. We have found a linear relation between log Q and VR, but not for BR or θ_{Bn}. This relation is energy dependent, since the log Q–VR slope smoothly changes from low to high energy. We cannot explain this energy dependence, because we have only modeled four events and because it varies from event to event. Our suspicion is that this relation only reflects part of the influence of the MHD variables at the cobpoint on the efficiency of the shock in the particle acceleration mechanisms. We expect that future improvements in the modeling of shock propagation and the study of a larger number of events will allow us to confirm (or reject) the existence of such relations. We have used the Q(VR) dependence derived to build up a synthetic flux profile to be compared with *Helios 2* observations, resulting in a very good agreement. We have discussed the influence of the corotation of the IMF tubes, concluding that depending on the type of particle event and the location of the observer, this effect cannot be ruled out in advance. Within 1 AU, however, it is not relevant in most situations.

The concept of the cobpoint allows us to quantify the evolution of the injection rate, Q, and the results derived confirm previous qualitative descriptions of its evolution (Kallenrode et al. 1993; Reames et al. 1996). We emphasize that the evolution of Q found is smoother than in previous studies. The dynamic evolution of the strength of the shock and in which part of the shock front the observer establishes magnetic connection throughout its expansion seem to be the main factors that determine the structure and shape of the particle events. Moreover, since the particle flux and anisotropy profiles are different at different energies, any

azimuthal dependence for Q along the shock front should be dependent on the energy and time. We have clearly established the influence of the shock (and of its evolution) on the flux profiles observed at different energy ranges by removing the effects of the particle transport.

Recently, some criticism regarding the adoption of the shock simulation has appeared (Kallenrode 1997b; Gopalswamy et al. 1998). We would like to point out that the shocks used in this work were chosen in such a way that the plasma conditions observed at different spacecraft were reasonably adjusted by the MHD modeling, and that a dynamical description of the shock (given by a MHD code) is better than a simple kinetic one. We have studied the influence of the initial shock conditions on the evolution of the injection rate, showing that the precise position of the cobpoint has a small influence on the evolution of Q, but that it can modify its quantitative dependence on VR. In our model, the shock is not described as a pressure pulse, and it does not need a flare explosion to drive it. On the contrary, we consider an explicit shock satisfying the computed Rankine-Hugoniot conditions. Moreover, it is not possible to have a flare explosion driving the shock and the CME, because, for example, two of the events (CM event and WS event, both well-known in the literature; i.e., Kahler 1992) are associated not with flare activity but with filament disappearances. We have assumed in all cases, regardless of the shock's solar origin and explicit formation, its existence at a certain distance (18 $R_\odot$), and further assumed that its shape and velocity fit plasma and IMF observations by two or more spacecraft. This fact does not exclude the acceleration of particles near the Sun by a coronal shock or in front of the CMEs; on the contrary, in some events they must coexist. In that sense, Cane (1997) comments: " Multispacecraft observations support the fact that in large events, particles are seen rather promptly from widespread regions. The widespread acceleration is difficult to reconcile in terms of latitudinal extents of CMEs and the longitudinal extents of interplanetary shocks at 1 AU." We plead for the existence of an injection of particles near the Sun, and an injection of particles from an expanding shock in the interplanetary medium, whose origin is probably the same shock propagating in a different medium and in a different way, or two shocks (Cane 1997). In some events, it is clear that the magnetic connection between the shock and the observer is established at some time (call it t_c or r_{start}; He95; Kallenrode 1997b) after the interplanetary shock has started to propagate, while the magnetic flux tubes may have been filled with energetic particles accelerated near the Sun.

To conclude these comments, we would like to point out that if for west events the magnetic connection between the observer and the shock exists from the beginning, while for east events this connection is established shortly before the passage of the shock (at 1 AU), a spectrum of values for the connecting time between zero and a few hours before the shock arrival must exist. The accuracy of its determination relies on how good the MHD simulation of the shock is, and on the details of how the coronal shock is produced and how it evolves to an interplanetary shock. Until such time as current ambiguities in shock modeling (such as the initial conditions and the width of the coronal shock) are removed, we rely on the observations of two or more spacecraft to fix the main characteristics of the propagating shock. A MHD model with the inner boundary conditions

set at $1 R_\odot$, which we expect to be available within the next few years, will be of great help to remove these uncertainties and to obtain more accurate values for the initial connecting time in west and central meridian events. In addition, it is necessary to study more individual events observed from different spacecraft, and to perform statistical analyses to confirm or reject our suggestion that the $Q(VR)$ relation, plus the cobpoint concept, provides a reliable tool for reproducing particle fluxes in this type of event.

REFERENCES

Balogh, A., et al. 1978, IEEE Trans. Geosc. Elec., G-16, 176
Balogh, A., González-Esparza, J. A., Forsyth, R. J., Burton, M. E., Goldstein, B. E., Smith, E. J., & Bame, S. J. 1995, Space Sci. Rev., 72, 171
Beeck, J., Mason, G. M., Marsden, R. G., Hamilton, D. C., & Sanderson, T. R. 1990, J. Geophys. Res., 95, 10279
Beeck, J., & Sanderson, T. R. 1989, J. Geophys. Res., 94, 8769
Beeck, J., & Wibberenz, G. 1986, ApJ, 311, 437
Behannon, K. W., Burlaga, L. W., & Hewish, A. 1991, J. Geophys. Res., 96, 21213
Bieber, J. W., Wanner, W., & Matthaeus, W. H. 1996, J. Geophys. Res., 101, 2511
Burlaga, L. F., Behannon, K. W., & Klein, L. W. 1987, J. Geophys. Res., 92, 5725
Cane, H. V. 1985, J. Geophys. Res., 90, 191
———. 1996, J. Geophys. Res., 101, 15533
———. 1997, AGU Geophys. Mono., 99, 205
Cane, H. V., Kahler, S. W., & Sheeley, N. R. 1986, J. Geophys. Res., 91, 13321
Cane, H. V., & Reames, D. V. 1990, ApJS, 73, 253
Cane, H. V., Reames, D. V., & von Rosenvinge, T. T. 1988, J. Geophys. Res., 93, 9555
———. 1991, ApJ, 373, 675
Cane, H. V., Sheeley, N. R., & Howard, R. A. 1987, J. Geophys. Res., 92, 9869
Chao, J. K., & Hshieh, K. C. 1984, Planet. Space Sci., 32, 641
Cliver, E. W. 1996, in High Energy Solar Physics, ed. R. Ramaty, N. Mandzhavidze, & X.-M. Hua (Woodbury: AIP), 45
Cliver, E. W., Kahler, S. W., Neidig, D. F., Cane, H. V., Richardson, I. G., Kallenrode, M.-B., & Wibberenz, G. 1995, Proc. 24th Int. Cosmic-Ray Conf. (Rome), 4, 257
Domingo, V., Sanahuja, B., & Heras, A. M. 1989, Adv. Space Res., 9(4), 195
Dryer, M. 1994, Space Sci. Res., 67, 363
Forman, M. A., & Webb, G. M. 1985, AGU Geophys. Mono., 34, 91
Gopalswamy, N., et al. 1998, J. Geophys. Res., 103, 307
Hasselmann, K., & Wibberenz, G. 1970, ApJ, 162, 1049
Heras, A. M., Sanahuja, B., Lario, D., Smith, Z. K., Detman, T., & Dryer, M. 1995, ApJ, 445, 497 (He95)
Heras, A. M., Sanahuja, B., Sanderson, T. R., Marsden, R. G., & Wenzel, K.-P. 1994, J. Geophys. Res., 99, 43
Heras, A. M., Sanahuja, B., Smith, Z. K., Detman, T., & Dryer, M. 1992, ApJ, 391, 359 (He92)
Jokipii, J. R. 1966, ApJ, 146, 480
———. 1971, Rev. Geophys. Space Phys., 9, 27
Kahler, S. W. 1992, ARA&A, 113, 197
Kahler, S. W., Cliver, E. W., Cane, H. V., McGuire, R. E., Stone, R. G., & Sheeley, N. R., Jr. 1986, ApJ, 302, 504
Kahler, S. W., Reames, D., & Sheeley, N. R., Jr. 1990, 21st Int. Cosmic-Ray Conf. (Adeleide), 5, 183
Kallenrode, M.-B. 1996, J. Geophys. Res., 101, 24393
———. 1997a, J. Geophys. Res., 102, 22335
———. 1997b, J. Geophys. Res., 102, 22347
Kallenrode, M.-B., & Wibberenz, G. 1997, J. Geophys. Res., 102, 22311
Kallenrode, M.-B., Wibberenz, G., Kunow, H., Müller -Mellin, R., Stolpovskii, V., & Kontor, N. 1993, Solar Phys., 147, 377

Klecker, B. 1983, Adv. Space Res. 2, 11, 285
Klecker, B., Scholler, M., & Hovestadt, D. 1983, ApJ, 251, 393
Kunow, H., Wibberenz, G., Green, G., Müller-Mellin, R., & Kallenrode, M. B. 1991, in Physics of the Inner Heliosphere II, ed. R. Schwenn & E. Marsch (Berlin: Springer), 243
Lario, D. 1997, Ph.D. thesis, Univ. Barcelona
Lario, D., Sanahuja, B., & Heras, A. M. 1995a, Proc. II SOLTIP Symp., Step GBRSC News, 5, 235
———. 1997, Adv. Space Res., 20, 1, 115
Lario, D., Sanahuja, B., Heras, A. M., Smith, Z., & Dryer, M. 1995b, Proc. 24th Int. Cosmic-Ray Conf. (Rome), 4, 385
Lee, M. A., & Ryan, J. M. 1986, ApJ, 303, 829
Miller, J. A., & Viñas, A. F. 1993, ApJ, 412, 386
Ng, C. K., & Reames, D. V. 1995, ApJ, 453, 890
Ng, C. K., & Wong, K.-Y. 1979, Proc. 16th Int. Cosmic-Ray Conf. (Kyoto), 5, 252
Parker, E. N. 1965, Planet. Space Sci., 13, 9
Pinter, S., Grigorieva, V. P., Kecskeméty, K., & Kudela, K. 1982, Proc. STIP Symp. on Solar/Interplanetary Intervals, ed. M. A. Shea, D. F. Smart, & S. M. P. McKenna-Lawlor (Huntsville: Book Crafters), 119
Reames, D. V. 1990, ApJ, 358, L63
Reames, D. V., Barbier, L. M., & Ng, C. K. 1996, ApJ, 446, 473
Reames, D. V., Barbier, L. M., von Rosenvinge, T. T., Mason, G. M., Mazur, J. E., & Dwyer, J. R. 1997a, ApJ, 483, 515
Reames, D. V., Cane, H. V., & von Rosenvinge, T. T. 1990, ApJ, 357, 259
Reames, D. V., Kahler, S. W., & Ng, C. K. 1997b, ApJ, 491, 414
Reinhard, R., van Nes, P., Sanderson, T. R., Wenzel, K.-P., Smith, E. J., & Tsurutani, B. 1983, Proc. 18th Int. Cosmic-Ray Conf. (Bangalore), 3, 162
Richardson, I. 1997, AGU Geophys. Mono., 99, 189
Roelof, E. C. 1969, in Lectures in High Energy Astrophysics, ed. H. Ögelman & J. R. Wayland (NASA SP-199), 111
Ruffolo, D. 1995, ApJ, 442, 861 (Ru95)
Sanahuja, B., & Domingo, V. 1982, Proc. STIP Symp. on Solar/Interplanetary Intervals, ed. M. A. Shea, D. F. Smart, & S. M. P. McKenna-Lawlor (Huntsville: Book Crafters), 311
Sanahuja, B., Domingo, V., Wenzel, K.-P., Joselyn, J. A., & Keppler, E. 1983, Sol. Phys., 84, 321
Sanderson, T. R., Reinhard, R., van Nes, P., & Wenzel, K.-P. 1985, J. Geophys. Res., 90, 19
Sanderson, T. R., Reinhard, R., & Wenzel, K.-P. 1981, J. Geophys. Res., 86, 4425
Sarris, E. T., Decker, R. B., & Krimigis, S. M. 1985, J. Geophys. Res., 90, 3961
Sheeley, N. R., Jr., Howard, R. A., Koomen, M. J., Michels, D. J., Schwenn, E., Muhlhauser, K. H., & Rosenbauer, H. 1985, J. Geophys. Res., 96, 163
Smith, Z. K., & Dryer, M. 1990, Sol. Phys., 129, 387
Tan, L. C., Mason, G. M., Klecker, B., & Hovestadt, D. 1989, ApJ, 345, 572
Valdés-Galicia, J. F. 1993, Sol. Phys., 62, 67
Vandas, M., Fischer, S., Odstrcil, D., Dryer, M., Smith, Z., & Detman, T. 1997, AGU Geophys. Mono., 99, 169
Watanabe, T., & Kakinuma, T. 1984, Adv. Space Res., 4(7), 331
Woo, R., & Schwenn, R. 1991, J. Geophys. Res., 96, 21227
Zalesak, S. T. 1979, J. Comput. Phys., 31, 335